Kinetic effects during the plane-front and dendritic solidification of multicomponent alloys

Paul Martin, Gildas Guillemot, Christopher Hareland, Peter Voorhees, Charles-André Gandin

Kinetic effects during the plane-front and dendritic solidification of multicomponent alloys

Paul Martin[a,b], Gildas Guillemot[b], Christopher A. Hareland[c], Peter W. Voorhees[c], Charles-André Gandin[b,*]

[a] *Safran Additive Manufacturing Campus, 105 Avenue Marcel Dassault, 33700 Mérignac, France*
[b] *MINES Paris, PSL University, CEMEF UMR CNRS 7635, CS10207, 06904 Sophia Antipolis, France*
[c] *Department of Materials Science and Engineering, Northwestern University, 2220 Campus Drive, Evanston, IL 60208, USA*

Abstract

A generalized model for the kinetics of a dendrite tip with a non-equilibrium interface is presented for multicomponent alloys. The model includes full coupling with thermodynamic databases to account for non-dilute non-ideal solutions, in addition to a full diffusion matrix in the liquid. The consequences of the computed non-equilibrium phase diagram boundaries on the dendrite tip kinetics are considered, and substantial deviations from existing theories are observed, especially in the case of zero solute drag. The model is applied to the rapid solidification of Inconel 718 (a nickel-based superalloy) and 316L (a stainless steel), which contain seven and five solute species, respectively. From the model, the phase diagram properties (i.e., partition coefficients and liquidus slopes) are able to be directly visualized as a function of velocity and observed to vary non-linearly and, in some cases, non-monotonically due to the combination of non-linear phase diagrams and kinetic effects. Finally, recent reports in the literature on the competition between the growth of ferrite and austenite from the melt in 316L are revisited with these new developments.

Graphical Abstract

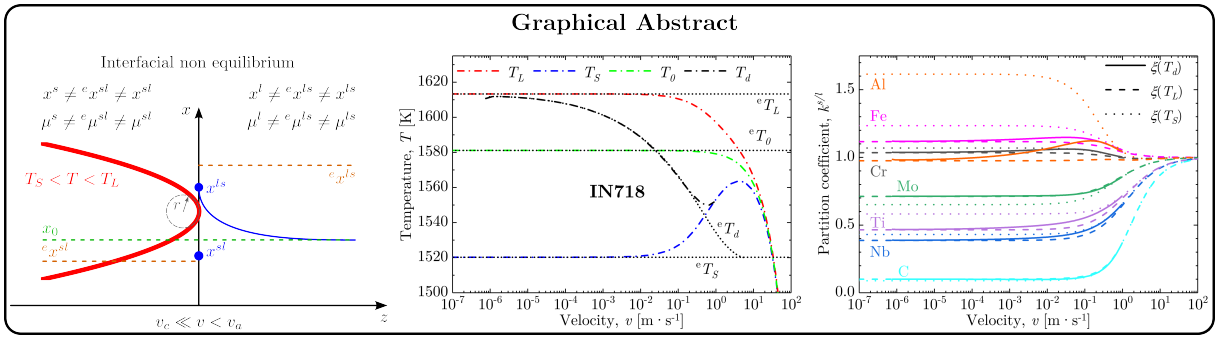

Keywords: Solidification, Thermodynamics, Kinetics, Dendrite, Multicomponent

*Corresponding author
Email address: Charles-Andre.Gandin@minesparis.psl.eu (Charles-André Gandin)

1. Introduction

Phase transformations in metal alloys influence the material microstructure and its properties. The complexity of the phenomena that occur during rapid solidification were addressed, both experimentally and theoretically, mainly during the last quarter of the twentieth century [1]. This includes non-equilibrium effects at a solid/liquid interface [2], which allowed phase diagram boundaries to be drawn as a function of the interface velocity [3, 4], as well as for the modeling of the non-equilibrium tip kinetics of dendrites [5, 6, 7], a ubiquitous type of microstructure formed during the solidification of metal alloys. However, investigations were primarily directed towards dilute binary alloys, i.e., those containing a small amount of a single solute element in the solvent metal, and the development of a theoretical basis for industrial (i.e., multicomponent) alloys was only just beginning [8, 9].

The necessity to characterize rapid solidification for multicomponent alloys is of prime importance to meet the future needs of industries. Rapid solidification induces a number of interfacial phenomena that occur during the growth of a solid "daughter phase", s, from a liquid "parent phase", l, at a given velocity, v $[\mathrm{m} \cdot \mathrm{s}^{-1}]$:

- *Attachment kinetics.* The transformation from a disordered liquid structure into an ordered solid structure is a process that dissipates energy, resulting in undercooling. This process is influenced by various factors, such as the cooling rate and the presence of atomic defects at the growing interface. The attachment kinetics are subject to a physical limit known as the "maximum speed of crystallization", denoted as v_0 $[\mathrm{m} \cdot \mathrm{s}^{-1}]$, which represents the maximum velocity of the interface at which crystallization can occur. When approaching this limit, an amorphous solid phase may form [10]. Note that this phenomenon is also expected in pure metals.

- *Solute drag.* The parent liquid phase at composition x_i^{ls} $[\mathrm{mol} \cdot \mathrm{mol}^{-1}]$ transforms into the growing solid phase of composition x_i^{sl} $[\mathrm{mol} \cdot \mathrm{mol}^{-1}]$, where the index $i \in \{1 : N-1\}$ denotes a solute component in an N-component alloy. When the interfacial region is at the composition of the parent phase, a trans-interface diffusion mechanism must occur in order to ensure that its composition adjusts to that of the growing phase. This process dissipates energy and is known as "full solute drag" [2, 3]. First presented for recrystallization [11], it was comprehensively characterized by Hillert and Sundman [12] to include solidification. However, "partial solute drag" models have also been proposed, in which the interfacial region is at an effective composition, x_i^{eff} $[\mathrm{mol} \cdot \mathrm{mol}^{-1}]$, which differs from the interfacial compositions of the bulk phases. The value of the effective composition is set by the "solute-drag parameter", λ_i, which acts as a weighting factor for the interfacial compositions of the solid and liquid [4, 13]. This parameter will be subsequently discussed in more detail. The importance of partial solute drag during rapid solidification has been well-established by recent molecular dynamics (MD) studies [14, 15, 16, 17].

- *Solute trapping.* As the solidification velocity increases, the process of trans-interface diffusion becomes limiting and the composition of the solid phase approaches that of the liquid phase. This phenomenon is referred to as "solute trapping". At very high velocities, the partition coefficient at the interface, $k_i^{s/l} = x_i^{sl}/x_i^{ls}$, can reach unity. In order to describe trans-interface diffusion in this

regime, Aziz *et al.* [2, 3] introduced the concept of the diffusion speed of the chemical species i through the interface, v_i^D [m · s^{-1}], using $v_i^D = D_i^I/\delta$, where D_i^I [m^2·s^{-1}] and δ [m] are the diffusion coefficient of solute species i within the interface and the thickness of the interface, respectively. It is worth noting that both solute drag and solute trapping result from the energy dissipation taking place at the interface due to trans-interface diffusion, although they are generally described as two distinct phenomena [4].

In parallel with the above considerations, models have been developed for dendrite tip kinetics. The first comprehensive theoretical framework for directional solidification was proposed by Kurz *et al.* [5]. It combined several previous studies, all of which assumed steady-state growth at a given velocity and in a constant temperature gradient, including $i-$ identification of a parabolic geometry as a good approximation for a dendrite tip [18], $ii-$ the Ivantsov solution for the diffusion problem ahead of a parabola [19], $iii-$ the stability analysis of a planar front [20], predicting the velocity interval [v_c, v_a] in which the planar interface becomes unstable, and $iv-$ the marginal stability criterion that approximates the dendrite tip radius as the minimum wavelength that destabilizes the solid/liquid interface [21], the expression for which is provided by an interfacial stability analysis [20]. The type of microstructure and the corresponding relationships between the interface compositions and chemical potentials are sketched in Figure 1 in the simple configuration of a binary alloy of solute composition x^0 with an equilibrium partition coefficient lower than unity, ${}^e k^{s/l} < 1$. With no interface velocity (Figure 1a), $v = 0\,\mathrm{m \cdot s^{-1}}$, full thermodynamic equilibrium between the solid and liquid phases is obtained, which is defined by uniform compositions, $x^{sl} = {}^e x^{sl}$ and $x^{ls} = {}^e x^{ls}$ with ${}^e k^{s/l} = x^{sl}/x^{ls} = {}^e x^{sl}/{}^e x^{ls}$, uniform and equal chemical potentials, $\mu^{sl} = \mu^{ls}$, and a planar interface. The latter properties adopt values given by the system temperature, T, that falls within the solidification interval of the alloy, i.e., between the equilibrium solidus temperature, ${}^e T_S$, and liquidus temperature ${}^e T_L$. It is worth noting that the minimum velocity below which a planar front is predicted (Figure 1b), v_c [m · s^{-1}], was already given by the constitutional supercooling criterion [22]. The maximum velocity above which the interface restabilizes (Figure 1e), v_a [m · s^{-1}], is due to the capillary force that counteracts the effect of the segregated solute. Hence, this latter velocity is not directly related to the above-mentioned phenomenon of complete solute trapping where $k^{s/l} = 1$ (sketched for a higher velocity in Figure 1f). For velocity $v_c \leq v \leq v_a$, cellular/dendritic microstructures form, shown in Figure 1c-d by a parabolic solid/liquid interface with tip radius r. One may also be able to identify an intermediate velocity below which interface equilibrium is maintained and the interface is still described by ${}^e k^{s/l}$ (Figure 1c) and above which the partition coefficient departs from equilibrium, $k^{s/l} > {}^e k^{s/l}$ (Figure 1d).

More recently, Hareland *et al.* [23] developed a partial solute drag model for non-equilibrium interfaces during phase transformations in concentrated multicomponent alloys, where partial solute drag is shown to affect both the temperature of the interface and the velocity-dependent distribution coefficients. Although it was only demonstrated for binary alloys, it is capable of dealing with industrial alloys, which we demonstrate in the present work. Similarly, Guillemot *et al.* [24] developed a thorough implementation of a model for multicomponent dendrite tip kinetics fully coupled with CALPHAD thermodynamic databases [25, 26]. This model was applied to Inconel 718, a Ni-base superalloy with seven solute species.

In this model, a full description of the phase diagram was used in direct calls to a CALPHAD database to determine the equilibrium calculations, which directly computed the effect of interfacial curvature on equilibrium and allowed the working tie line for the solid/liquid interface at the dendrite tip to be accessed. A full diffusion matrix was also accounted for using the multicomponent stability analysis (still assuming growth at marginal stability [21]) and the analytical expression of the diffusion field around a paraboloid of revolution provided by Hunziker [27]. However, this advanced multicomponent dendrite tip model relied on the assumption of thermodynamic equilibrium at the solid/liquid interface. Most recently, Hariharan *et al.* [28] developed CALPHAD implementations for several existing sets of interfacial response functions and dendritic growth models, although their implementation was limited to diagonal diffusion matrices and did not consider partial solute drag.

With the recent renewed interest in rapid solidification, primarily due to the advent of additive manufacturing (AM) processes, coupling the thermodynamics of a non-equilibrium solid/liquid interface with the dendrite tip kinetics for multicomponent alloys is required. Hereafter, we couple the above-mentioned partial-drag model [23] and dendrite tip kinetics model [24]. We first present the kinetic equations governing the non-equilibrium interface — the "velocity response function" (VRF) and the "concentration response functions" (CRF) — which allows the non-equilibrium phase boundaries, such as the liquidus temperature, T_L, and solidus temperature, T_S, to be calculated as a function of velocity, enabling the construction of so-called "kinetic phase diagrams". The methodology to compute the velocity-dependent T_0 line is also provided, as it is the high-velocity limit for both the non-equilibrium T_L and T_S curves. We then recall the equations for the dendrite tip kinetics and explain the methodology adopted in the coupling with non-equilibrium interface conditions. Results are first described for a simple Ag–Cu binary alloy before applying the model to the Ni-base superalloy Inconel 718 and grade 316L stainless steel.

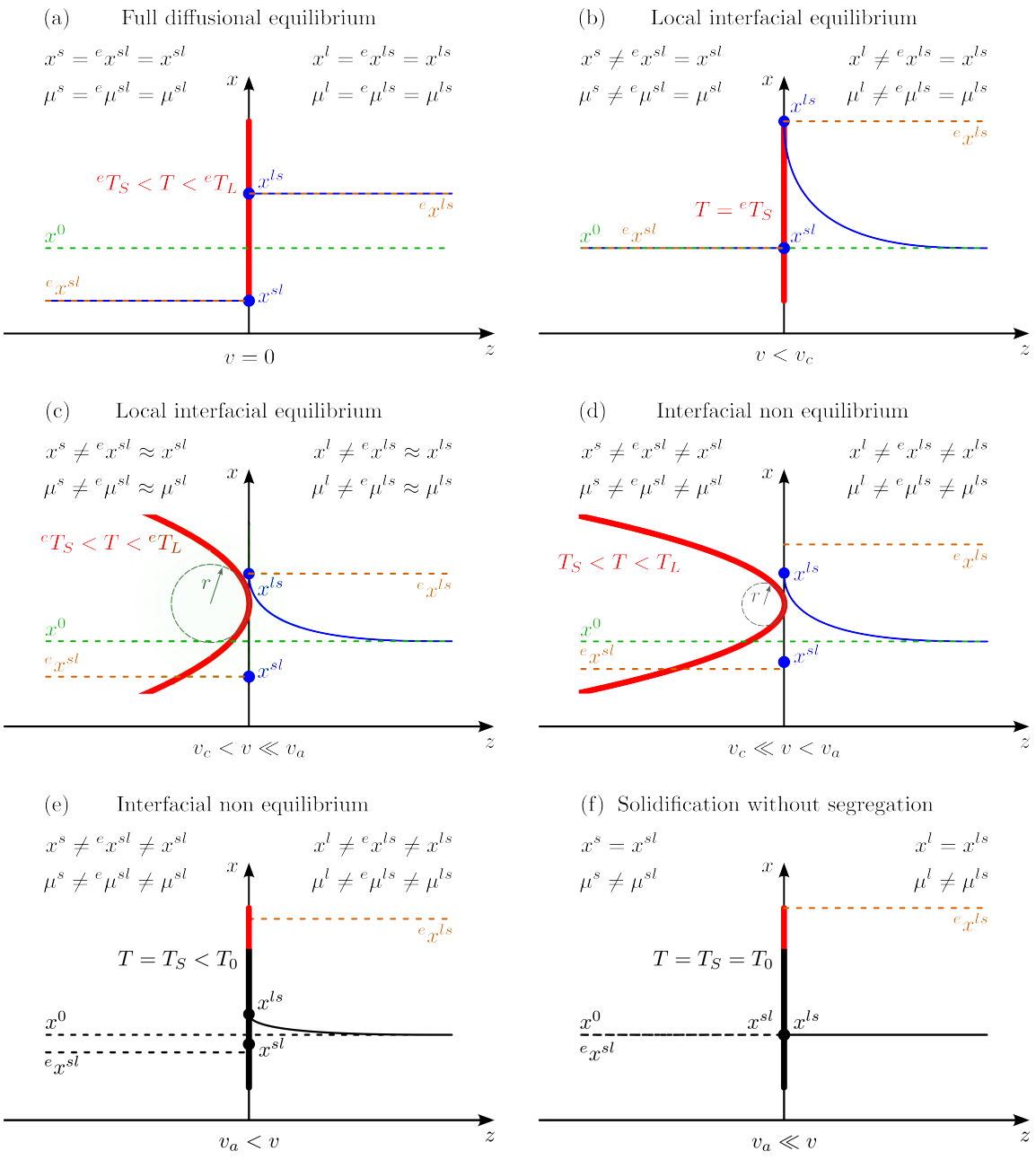

Figure 1: Schematics of a solidification interface growing at steady state for a binary alloy of (dashed green) solute composition x^0 and partition coefficient at equilibrium lower than unity, with (red) morphology and temperature, (blue) composition profiles along the z-direction, x, and (dashed yellow) equilibrium compositions. Chemical potentials, μ, are also given for (a) a static planar interface and full thermodynamic equilibrium, $v = 0\,\mathrm{m \cdot s^{-1}}$, (b) $v < v_c$ plane front with interface equilibrium only, (c) $v_c < v \ll v_a$ parabolic dendrite tip with interface equilibrium, (d) $v_c \ll v < v_a$ parabolic dendrite tip with non-equilibrium effects, (e) $v_a < v$ planar front with non-equilibrium effect and interface segregation and (f) ($v_a \ll v$) partitionless non-equilibrium planar front. Notations distinguishes between equilibrium quantities, ${}^e\{.\}$, at the interface, $\{.\}^{sl}$ and $\{.\}^{ls}$, respectively in the solid and liquid phases, and $\{.\}^s$ and $\{.\}^l$ averaged in the solid and liquid phases, respectively.

2. Modeling

The thermodynamics of a non-equilibrium solid/liquid interface including partial solute drag is first formulated for a multicomponent alloy, followed by a model that describes the growth kinetics of a constrained dendrite tip. The methodology for coupling the two sets of equations together with computed non-equilibrium thermodynamics is then introduced.

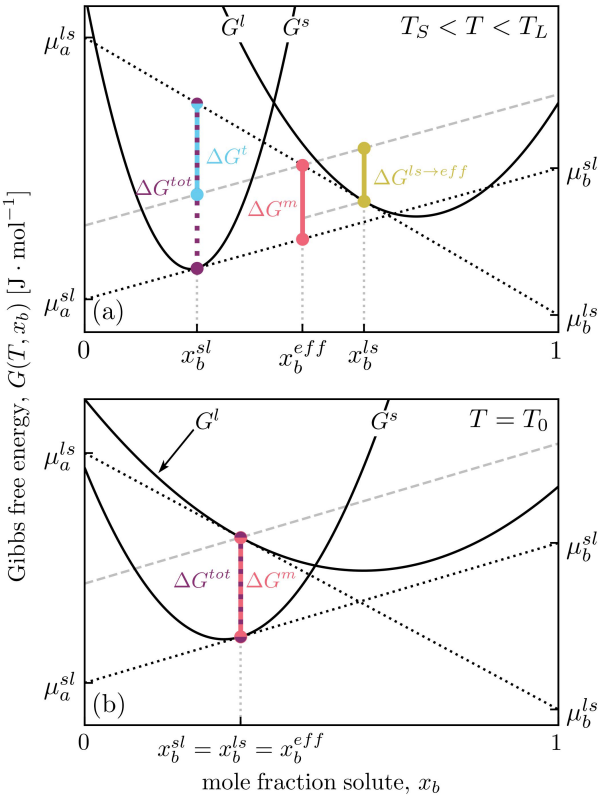

Figure 2: Graphical constructions for solidification of a binary alloy (solvent = a, solute = b) showing the dissipative processes at fixed temperature, velocity, and pressure for (a) the partial-solute-drag model in which the interface can adsorb material at $x_b^{eff} \neq x_b^{ls}$ [23] and (b) its extreme configuration for partitionless solidification, where $x_b^{sl} = x_b^{ls} = x_b^{eff}$, $\Delta G^t = 0$, $\Delta G^{tot} = \Delta G^m$ with $\lambda \neq 0$ and $v^D/v_0 \ll 1$.

2.1. *Non-equilibrium solid/liquid interface*

The non-equilibrium interface model with partial solute drag used hereafter was recently developed by Hareland *et al.* for multicomponent alloys, yet was only demonstrated for binary alloys [23]. It is based on the rate of Helmholtz free energy dissipation. In an N-component alloy (where the solutes are components $i \in \{1 : N-1\}$ and the solvent is component $i = N$, such that $\sum_{i=1}^{N} x_i^\phi = 1$ in any phase ϕ), the effect of partial solute drag is introduced by considering the $(N-1)$ independent "effective compositions" of the sharp interface, x_i^{eff}:

$$x_i^{eff} = \lambda x_i^{ls} + (1-\lambda) x_i^{sl} \quad \forall\, i \in \{1 : N-1\} \tag{1}$$

where λ [mol $\cdot$ mol^{-1}] is the "solute-drag parameter". We note that the dissipation relation used to derive the current formulation uses a single value of λ that applies to all species [23].

Figure 2a provides graphical schematics of the dissipation processes in binary alloys at fixed temperature and pressure. The total energy dissipation, ΔG^{tot}, is the sum of the contribution due to crystallization, or "interface migration", ΔG^{m}, and the contribution from solute redistribution, or "trans-interface diffusion", ΔG^{t}. The amount of energy given by $\Delta G^{ls \rightarrow eff}$ in Figure 2 represents the additional energy required for crystallization to occur at x_i^{eff} (i.e., partial solute drag) instead of x_i^{ls} (i.e., full solute drag). For multicomponent alloys, the total Gibbs free energy change for solidification is given by [8, 29]:

$$\Delta G^{tot} = \sum_{i=1}^{N} x_i^{sl} [\![\mu_i]\!] \tag{2}$$

where $[\![\mu_i]\!] = \mu_i^{ls} - \mu_i^{sl}$ is the difference in chemical potential between the liquid phase and the solid phase at their respective interfacial compositions. The expressions for ΔG^{m} and ΔG^{t} in the present model are analogous to those in Refs. [8, 29], but x_i^{ls} is replaced by x_i^{eff} when considering partial solute drag [23]:

$$\Delta G^{m} = \sum_{i=1}^{N} x_i^{eff} [\![\mu_i]\!] \tag{3}$$

$$\Delta G^{t} = \sum_{i=1}^{N} \left(x_i^{sl} - x_i^{eff} \right) [\![\mu_i]\!] \tag{4}$$

Note that the total free energy, $\Delta G^{tot} = \Delta G^{m} + \Delta G^{t}$, is independent of the amount of solute drag, i.e., the value of x_i^{eff} [23]. If we consider the case of full solute drag ($\lambda = 1$), we have $x_i^{eff} = x_i^{ls}$ from Eq. (1), causing Eqs. (3) and (4) to recover the expressions in Refs. [8, 29], but ΔG^{tot} is still given by Eq. (2).

These Gibbs free energy changes are related to the driving forces for these energy-dissipating processes, which are in turn linked to the associated interfacial fluxes through a set of kinetic equations known as "Interfacial Response Functions" (IRFs) [30, 23]. With the additional developments to the derivation in Hareland *et al.* [23] presented in Appendix A, the following IRFs—a Velocity Response Function (VRF) and $(N-1)$ Concentration Response Functions (CRFs)—are obtained for a multicomponent alloy:

$$v = \frac{v_0}{RT} \sum_{i=1}^{N} x_i^{eff} [\![\mu_i]\!] \tag{5}$$

$$v \left(x_i^{eff} - x_i^{sl} \right) = \frac{x_i^{eff} v_i^{D}}{RT} \left(\sum_{j=1}^{N} x_j^{eff} [\![\mu_j]\!] - [\![\mu_i]\!] \right) \quad \forall\, i \in \{1 : N-1\} \tag{6}$$

It is important to note that, although Eqs. (1) and (6) are also valid for the solvent ($i = N$), only the equations for the $(N-1)$ independent species (i.e., the solutes) are required. For given kinetic parameters λ, v_0, and v_i^{D}, this system of IRFs can be solved to determine the non-equilibrium phase boundaries, i.e., the kinetic phase diagram, as discussed in Section 2.3.

We now draw attention to the case of "partitionless solidification", which corresponds to identical solid and liquid interfacial compositions, $x_i^{sl} = x_i^{ls}$ $(= x_i^{eff})$. In this situation, no energy is dissipated by trans-interface diffusion, i.e., $\Delta G^t = 0$, so the total free energy change of solidification is dissipated by the migration of the interface, $\Delta G^{tot} = \Delta G^m$. This case is shown in Figure 2b. In this limit, Eq. (5) can be rewritten as

$$T_0 = \frac{v_0}{Rv} \sum_{i=1}^{N} x_i^{sl} [\![\mu_i]\!] \tag{7}$$

where T_0 defines the "partitionless temperature". While T_0 is velocity-dependent, it is independent of the solute-drag parameter, λ, and the trans-interface diffusion speeds, v_i^D, because the exchange of solute at the interface vanishes.

We note that the present definition of T_0 differs from the one introduced by Baker and Cahn [31] and commonly found in the literature [3, 32]. The latter temperature, hereafter denoted by ${}^eT_0$, is defined by the point at which the free energies of the solid and liquid are equal, i.e., $G^l({}^eT_0) = G^s({}^eT_0)$. The fact that partitionless solidification is found at ${}^eT_0$, i.e., $x_i^{sl}({}^eT_0) = x_i^{ls}({}^eT_0)$, is a consequence of this definition. Because the Gibbs free energy curves are independent of velocity, the value of ${}^eT_0$ is also independent of velocity, which is illustrated in Figure 6 of Reference [3]. Figure 2b illustrates the more general case described by Eq. (7), where $x_i^{sl}(T_0) = x_i^{ls}(T_0)$ when $G^l(T_0) \neq G^s(T_0)$. However, we note that the low-velocity limit of Eq. (7) recovers the definition of the ${}^eT_0$ temperature, as the summation in the numerator of Eq. (7) must tend towards zero to obtain a finite value of T_0 when $v \ll v_0$. With the condition $x_i^{ls} = x_i^{sl}$, this leads to $G^l(x_i^{ls}, T_0) = G^s(x_i^{sl}, T_0)$ and thus $T_0 = {}^eT_0$. In Section 3, we shall furthermore illustrate that, for $\lambda \neq 0$ and $v_i^D/v_0 \ll 1$, the definition of partitionless solidification at T_0 by Eq. (7) recovers the expected behavior at high velocity, i.e., $T_L = T_S = T_0$. Additionally, in the limiting case of $\lambda = 0$ (no solute drag), Eq. (1) gives $x_i^{eff} = x_i^{sl}$, reducing Eqs. (5) and (6) to $[\![\mu_i]\!] = RTv/v_0 \ \forall \ i \in \{1 : N\}$. If Figure 2b were redrawn under this condition, the magnitudes of the slopes of the free energy curves at the interfacial compositions would be equal, despite the departure from thermodynamic equilibrium and the common-tangent construction.

2.2. Dendrite tip kinetics

The model used hereafter for dendrite tip growth kinetics is derived from the recent work of Guillemot *et al.* [24], which extended the developments by Hunziker [27] that were limited to linear phase diagrams (i.e., constant liquidus slopes and partition coefficients) and uncoupled with thermodynamic equilibrium calculations. In the present model, a multicomponent alloy of nominal molar composition $\mathbf{x^0} = (x_i^0)_{1 \leq i \leq N-1}$ $[\text{mol} \cdot \text{mol}^{-1}]$ is considered. A dendrite tip of curvature radius r [m] grows steadily at a given velocity, v, and temperature, T_d [K], in a fixed temperature gradient, G $[\text{K} \cdot \text{m}^{-1}]$, which is imposed in both the solid and liquid phases along the main growth direction of the dendrite. Solute transfer in the liquid phase is solely governed by diffusion, with a diffusion matrix $\mathbf{D} = (D_{ij})_{1 \leq (i,j) \leq N-1}$ $[\text{m}^2 \cdot \text{s}^{-1}]$. Unlike the presentation in Reference [24], equations are written with mole fractions rather than mass fractions. This not only ensures compatibility with Section 2.1, but is also a requirement when obtaining the full diffusion matrix from thermodynamic databases [25, 26], as explained in Appendix B.

2.2.1. Solute diffusion

The composition field in the liquid phase surrounding the growing dendrite tip is provided by the solution of the mass conservation equation defined in paraboloidal coordinates [18]. While it is available for nonaxisymmetric dendritic growth [33, 34], we shall hereafter assume an axisymmetric paraboloidal dendrite tip. The solution to the latter was originally proposed by Ivantsov [19] and later extended to multicomponent alloys [27]. Considering the compositions at the dendrite tip, $\mathbf{x^{ls}} = (x_i^{ls})_{1\leq i\leq N-1}$ (resp. $\mathbf{x^{sl}} = (x_i^{sl})_{1\leq i\leq N-1}$) in the liquid (resp. solid) phase, the following relations are obtained after mathematical resolution:

$$x_i^{ls} = x_i^0 + \sum_{j=1}^{N-1}\sum_{k=1}^{N-1} \left(x_k^{ls} - x_k^{sl}\right)\, U_{ij}\, U_{jk}^{-1}\, \mathrm{Iv}(Pe_j) \quad \forall\, i \in \{1 : N-1\} \tag{8}$$

where $\mathbf{U}_{.j}$ is the $j-$th unit eigenvector (with components $(U_{ij})_{1\leq(i,j)\leq N-1}$) of the diffusion matrix, $\mathbf{D}$. Consequently, the matrix $\mathbf{U}$ is the transformation matrix of $\mathbf{D}$ composed of its eigenvectors. The eigenvalues of this diffusion matrix are the $\mathbf{B} = (B_i)_{1\leq i\leq N-1}$ values, and are associated to the solutal Péclet numbers, $Pe_i = rv/(2B_i)$. Lastly, $\mathrm{Iv}(x) = x\,\exp(x)\,\mathrm{E}_1(x)$ is the Ivantsov function, where $\mathrm{E}_1(x)$ is the exponential integral.

The dendrite tip temperature, T_d, is determined by $i-$ the interfacial composition of the liquid, $\mathbf{x^{ls}}$, $ii-$ the excess Gibbs free energy due to curvature in the solid phase (i.e., the Gibbs-Thomson effect), ΔG_κ^s [$\mathrm{J\cdot mol^{-1}}$], $iii-$ departure from thermodynamic equilibrium at the solid/liquid interface at large velocities. A general formulation can be written as:

$$T_d = \mathrm{F_L}\left(\mathbf{x^{ls}}, \Delta G_\kappa^s, v\right) \tag{9}$$

where the excess Gibbs free energy is proportional to the curvature at the dendrite tip, $\kappa = 2/r$ [$\mathrm{m^{-1}}$], and provided by the relation $\Delta G_\kappa^s = \kappa\gamma V_M^s$, where γ [$\mathrm{J\cdot m^{-2}}$] is the interfacial energy and V_M^s [$\mathrm{m^3{\cdot}mol^{-1}}$] is the molar volume of the solid phase. Similarly, the set of compositions in the solid phase is dependent on the liquid compositions, excess Gibbs free energy, and interface velocity, and a similar relation can be written:

$$\mathbf{x^{sl}} = \mathrm{F_S}\left(\mathbf{x^{ls}}, \Delta G_\kappa^s, v\right) \tag{10}$$

It must be noted that $\mathbf{x^{sl}}$ and $\mathbf{x^{ls}}$ are not provided by tie-lines corresponding to thermodynamic equilibrium, as they both depend on the interface velocity. This is the main difference with Ref. [24].

2.2.2. Stability criterion

The microsolvability theory [35, 36, 37, 38] or phase-field simulations [39, 40] should be used to compute the length scale associated with the dendrite tip radius as a function of the strength of the crystal anisotropy. In the following, a simple form is used, $(r/\lambda_{min})^2 = \sigma^*/\sigma$ with $\sigma^* = (2\pi)^{-2}$, simply stating that the radius at the dendrite tip is proportional to the minimal unstable wavelength of a perturbation developing at the solid/liquid interface, λ_{min} [m]. This formulation is a pragmatic choice, as the constant σ is often unknown for multicomponent alloys. The condition $\sigma = \sigma^*$ corresponds to the marginal stability criterion [41], which directly states that $r = \lambda_{min}$. The value of λ_{min} can be evaluated

following the original stability analysis of Mullins and Sekerka [20] extended to dilute multicomponent alloys [42, 9] and including cross-diffusion of the chemical species in the liquid. Finally, the mathematical expressions given by Hunziker [27] are applied to a non-dilute multicomponent alloy using direct calls to thermodynamic equilibrium calculations [24]. The following equation for the so-called "neutral stability curve" provides the wavenumber, ω [m^{-1}], at the boundary between stable and unstable perturbations, which corresponds to $\lambda_{min} = 2\pi/\omega$:

$$\sum_{i=1}^{N-1} m_i^{ls} \sum_{j=1}^{N-1} U_{ij} F_j - \Gamma\omega^2 - G = 0 \tag{11}$$

where $(m_i^{ls})_{1\leq i\leq N-1}$ [$\mathrm{K\cdot mol.\%^{-1}}$] are the liquidus slopes of the kinetic phase diagram at the temperature and composition of the s/l interface, Γ [$\mathrm{K\cdot m}$] is the Gibbs-Thomson coefficient of the alloy, and the $(F_i)_{1\leq i\leq N-1}$ coefficients are solutions of the following system [24]:

$$\sum_{j=1}^{N-1} \left[U_{kj}\,\zeta_j - 2\sum_{i=1}^{N-1} U_{ij}\,K_{ki} \right] F_j = -\sum_{j=1}^{N-1} v\,\frac{U_{kj}\,A_j}{B_j}\,\zeta_j \quad \forall\, k \in \{1 : N-1\} \tag{12}$$

where the $(\zeta_i)_{1\leq i\leq N-1}$ coefficients are given by:

$$\zeta_i = 1 - \sqrt{1 + \left(\frac{2\omega B_i}{v}\right)^2} \quad \forall\, i \in \{1 : N-1\} \tag{13}$$

The $\mathbf{A}$ vector, with coefficients $(A_i)_{1\leq i\leq N-1}$, depends on the concentration difference at the solid/liquid interface, $\mathbf{\Delta x} = \mathbf{x^{ls}} - \mathbf{x^{sl}}$ [24]:

$$\mathbf{A} = \mathbf{U^{-1}} \cdot \mathbf{\Delta x} \tag{14}$$

The $\mathbf{K} = (K_{ij})_{1\leq(i,j)\leq N-1}$ [$\mathrm{mol\cdot mol^{-1}}$] matrix in Eq. (12) defines the partitioning of solute species. The element K_{ij} represents the effect of a change in the liquid composition of element j on the solid composition of element i at the solid/liquid interface:

$$K_{ij} = \left.\frac{\partial x_i^{sl}}{\partial x_j^{ls}}\right|_{x_{k\neq j}^{ls}} \quad \forall\, (i,j) \in \{1 : N-1\} \tag{15}$$

Note that these coefficients are not the equilibrium partition coefficients of the chemical elements, but depend on the non-equilibrium effects taking place at the interface, i.e., the kinetic phase diagram. In this analysis, these velocity-dependent quantities, as well as the velocity-dependent liquidus slopes, are substituted into the standard expression for the neutral stability curve obtained from a stability analysis at local interfacial equilibrium. The stability analysis by Coriell, Sekerka, and McFadden [43, 44, 45] shows that this approach is valid for a binary alloy with non-equilibrium interfaces. Performing the analysis for a binary alloy shows that any derivatives with respect to velocity that appear when considering velocity-dependent quantities will be multiplied by the growth rate of the perturbation, and will thus disappear in the neutral stability curve defined by a zero growth rate, so it is reasonable to assume that this approach is also valid for multicomponent alloys. Additionally, the velocity-dependent derivatives disappear for the

neutral stability curve in the multicomponent stability analysis of Ludwig et al. [46], further validating this approach. Solving Eqs. (11)–(15) gives the minimum unstable wavelength for a planar interface, and thus provides an estimate of the dendrite tip radius.

2.3. Calculating non-equilibrium thermodynamic quantities

The interface response functions presented in Section 2.1 can be used to calculate quantities from phase diagrams under non-equilibrium thermodynamic conditions, i.e., high solidification rates. The systems of equations used to calculate the quantities discussed hereafter are summarized in Table 1. Regardless of the unknown variables, the strategy used to solve the appropriate system of equations is based on the Newton-Raphson algorithm, which requires the derivatives of each equation with respect to each unknown variable.

- *Kinetic phase diagram.* To compute the kinetic phase diagram for an N-component alloy, the unknown variables are the $2N-2$ interfacial solid/liquid compositions, $\mathbf{x^{ls}}$ and $\mathbf{x^{sl}}$, that define the phase boundaries at a given temperature. For fixed values of the kinetic parameters (λ, v_0, v_i^D) at a given value of the temperature, T, and the velocity, v, the system of equations is composed of one VRF (Eq. 5) and $N-1$ CRFs (Eqs. 6). However, this leads to an underdetermined system of N equations in $2N-2$ unknowns, so a method of choosing the values for $N-2$ unknowns is required when $N>2$. Solving this system over a range of temperatures allows the phase diagram to be constructed.

- *Kinetic liquidus and solidus.* It is simpler to compute the kinetic liquidus and solidus temperatures for a given composition and velocity; for a nominal alloy composition, $\mathbf{x^0}$, we have $\mathbf{x^{ls}}=\mathbf{x^0}$ on the kinetic liquidus and $\mathbf{x^{sl}}=\mathbf{x^0}$ on the kinetic solidus. For fixed values of the kinetic parameters (λ, v_0, v_i^D), velocity, v, and nominal composition, $\mathbf{x^0}$, the system has N unknowns: the temperature, T, and $N-1$ interfacial compositions, $\mathbf{x^{sl}}$ (resp. $\mathbf{x^{ls}}$) for the liquidus (resp. solidus). After solving this system, the partition coefficients, $k_i^{s/l}=x_i^{sl}/x_i^{ls}$, and liquidus slopes, $m_i^{ls}=\partial T/x_i^{ls}|_{x_{j\neq i}}$, can be calculated at both the liquidus and solidus temperatures from the compositions at these temperatures. In general, non-linear phase boundaries will result in different values of these quantities at the liquidus and solidus temperatures.

- *T_0 curve.* To obtain the T_0 curve, only the modified VRF from Eq. (7) is needed. Because the T_0 transformation is partitionless, we take $\mathbf{x^0}=\mathbf{x^{ls}}=\mathbf{x^{sl}}$. For fixed values of the kinetic parameter v_0, velocity, v, and nominal composition, $\mathbf{x^0}$, the partitionless temperature, T_0, is the only unknown quantity.

2.3.1. Integration in the model of dendrite tip kinetics

To incorporate kinetic effects into the calculation of the working point of a dendrite tip, it is necessary to replace any uses of classical thermodynamic equilibrium with calls to the solution of the system of IRFs (one VRF and $N-1$ CRFs). For example, the interfacial compositions x_i^{sl} can be calculated with the same methodology used to compute the kinetic liquidus described above. Additionally, quantities corresponding to derivatives along the kinetic phase diagram, i.e., the non-equilibrium liquidus slopes

Output property	Inputs	Unknowns	(number)	Equations	(number)
Phase diagram	λ, v_0, v_i^D, v, T	$\mathbf{x^{ls}}$, $\mathbf{x^{sl}}$	$(2N-2)$	(5), (6)	(N)
Liquidus	λ, v_0, v_i^D, v, $\mathbf{x^0}$ $(=\mathbf{x^{ls}})$	$\mathbf{x^{sl}}$, T	(N)	(5), (6)	(N)
Solidus	λ, v_0, v_i^D, v, $\mathbf{x^0}$ $(=\mathbf{x^{sl}})$	$\mathbf{x^{ls}}$, T	(N)	(5), (6)	(N)
T_0 line	v_0, v, $\mathbf{x^{ls}}$ $(=\mathbf{x^{sl}}=\mathbf{x^0})$	T	(1)	(7)	(1)

Table 1: Systems of equations used to obtain non-equilibrium thermodynamic properties, with the lists of inputs and outputs [4, 29, 23].

and segregation matrix, are calculated numerically using the system of IRFs. With this approach, the model of dendrite tip kinetics developed in Ref. [24] can be improved at high velocities by accounting for non-equilibrium effects at the interface. We note that removing the velocity dependence from Eqs. (9) and (10) when solving the equations in Section 2 retrieves the local equilibrium results in Ref. [24] (although with slight differences due to the use of weight percents in Ref. [24], as discussed in Appendix B).

The present model directly computes the tip temperature of the dendrite by simultaneously accounting for interfacial curvature, non-equilibrium kinetic effects, and solute diffusion. These three effects contribute to the total undercooling of the dendrite tip, $\Delta T_d = {}^eT_L - T_d$ [K], which is defined with respect to the equilibrium liquidus temperature of the alloy with a planar front, ${}^eT_L = \mathrm{F_L}\left(\mathbf{x^0}, \Delta G^s_\kappa = 0, v = 0\right)$ [K]. However, the model is never explicitly based on expressions for the curvature undercooling, ΔT_κ [K], kinetic undercooling, ΔT_v [K], and solutal undercooling, ΔT_χ [K], as is usually found in the literature [5], because neither a linear phase diagram nor an ideal dilute system is assumed. For illustrative purposes, these three contributions to ΔT_d can be individually evaluated. For instance, it is possible to remove the effect of the excess Gibbs free energy due to curvature and recompute the working point of the dendrite tip, which gives an estimate of the curvature undercooling. Similar procedures can be used to obtain the kinetic undercooling and the solutal undercooling. With the dendrite tip temperature given by Eq. (9), we proceed as follows:

$$\Delta T_d = {}^eT_L - T_d = \Delta T_v + \Delta T_\kappa + \Delta T_\chi \tag{16}$$

$$\Delta T_v = T_L\left(\mathbf{x^0}, \Delta G^s_\kappa = 0, v = 0\right) - T_v\left(\mathbf{x^0}, \Delta G^s_\kappa = 0, v\right) \tag{17}$$

$$\Delta T_\chi = T_v\left(\mathbf{x^0}, \Delta G^s_\kappa = 0, v\right) - T_\chi\left(\mathbf{x^{ls}}, \Delta G^s_\kappa = 0, v\right) \tag{18}$$

$$\Delta T_\kappa = T_\chi\left(\mathbf{x^{ls}}, \Delta G^s_\kappa = 0, v\right) - T_d \tag{19}$$

3. Discussion in the context of binary alloys

To illustrate the physics of the above model, we examine the binary Ag–Cu system with free energies from the thermodynamic database TCAL4 [47]. The other parameters necessary to compute the kinetic phase diagram boundaries are the solute-drag parameter, the maximum crystallization speed, and the trans-interface diffusion speed, all listed in the first part of Table 2.

Property	Symbol	Value	Unit	Ref
Thermodynamic database		TCAL4		[47]
Solute-drag parameter	λ	0., 1.	$[\mathrm{mol}\cdot\mathrm{mol}^{-1}]$	[23]
Maximum crystallisation speed	v_0	850	$[\mathrm{m}\cdot\mathrm{s}^{-1}]$	[23]
Trans-interface diffusion speed	v^D	0.4	$[\mathrm{m}\cdot\mathrm{s}^{-1}]$	[23]
Mobility database		MOBAL3		[48]
Equilibrium liquidus temperature	${}^eT_L$	1189.2	[K]	[47]
Diffusion of Cu in liquid at ${}^eT_L$	D_{Cu}	$7.61\cdot10^{-9}$	$[\mathrm{m}^2\cdot\mathrm{s}^{-1}]$	
Interfacial energy	γ	0.168	$[\mathrm{J}\cdot\mathrm{m}^{-2}]$	[49]
Selection parameter	σ	$(2\pi)^{-2}$	$[-]$	[5]
Temperature gradient	G	10^7	$[\mathrm{K}\cdot\mathrm{m}^{-1}]$	[5]

Table 2: Material properties for alloy Ag–5 wt% Cu. The first set of properties is used to compute the phase diagram boundaries with the PDM [23] and CGM [3, 4] models. Both sets of parameters are needed for the dendrite tip kinetics [24].

In the following analysis, we compare the interfacial response functions of the present model, which we will hereafter refer to as the "Partial-Drag Model" (PDM), to the version of the "Continuous-Growth Model" (CGM) incorporating partial solute drag by Aziz and Boettinger [4] and its recent extension to multicomponent alloys by Du et al. [29]. The VRF and CRFs for binary and multicomponent alloys from both models are summarized in Table A.1 of Appendix A. We note two key differences between the PDM and the CGM (see Ref. [23] for further discussion). First, the CGM describes the flux of atoms with an Arrhenius equation, while the PDM assumes linear kinetics, as is common in typical force-flux laws found in irreversible thermodynamics. Second, because the PDM self-consistently incorporates the effect of partial solute drag, the effective concentration, x_i^{eff}, appears in both the VRF and CRFs of the PDM, while it only appears in the VRF of the CGM[1].

3.1. Planar interface kinetics (phase boundaries)

Figure 3 shows the full metastable binary phase diagram calculated for the Ag–Cu system using the IRFs with the parameters listed in Table 2. Both the "zero-drag" (top row: $\lambda = 0 \implies \Delta G^t = 0$) and "full-drag" (bottom row: $\lambda = 1$) cases are shown at an interfacial velocity of $v = 0.1\,\mathrm{m}\cdot\mathrm{s}^{-1}$. At this velocity, the effects of attachment kinetics are not yet significant (i.e., $v \ll v_0$). Because of this, the zero-drag case of the PDM (top left) reproduces the equilibrium phase boundaries, as expected, although the zero-drag limit of the CGM (top right) does not. Moving to the full-drag case, the liquidus temperature is depressed from the zero-drag case in both models (bottom row). This occurs because increasing λ from zero requires the redistribution of solute across the interface, consuming energy that that would otherwise be used to move the interface. Additionally, the regions of solid spinodal decomposition are also shown

[1]One could also notice that, when combining Eqs 14a and 14b in Reference [29], Du et al. consider a mathematical approximation to derive their Eq. 14c. It is based on the assumption that the concentration of each component is very low compared to the concentration of the solvent. This should not be the case when dealing with non-dilute alloys.

in Figure 3 (sparsely dotted black curve); while the PDM (left) shows retrograde behavior of the solidus curves at the velocity for both the zero- and full-drag limits, the CGM (right) does not reproduce the retrograde behavior in either limit at this velocity.

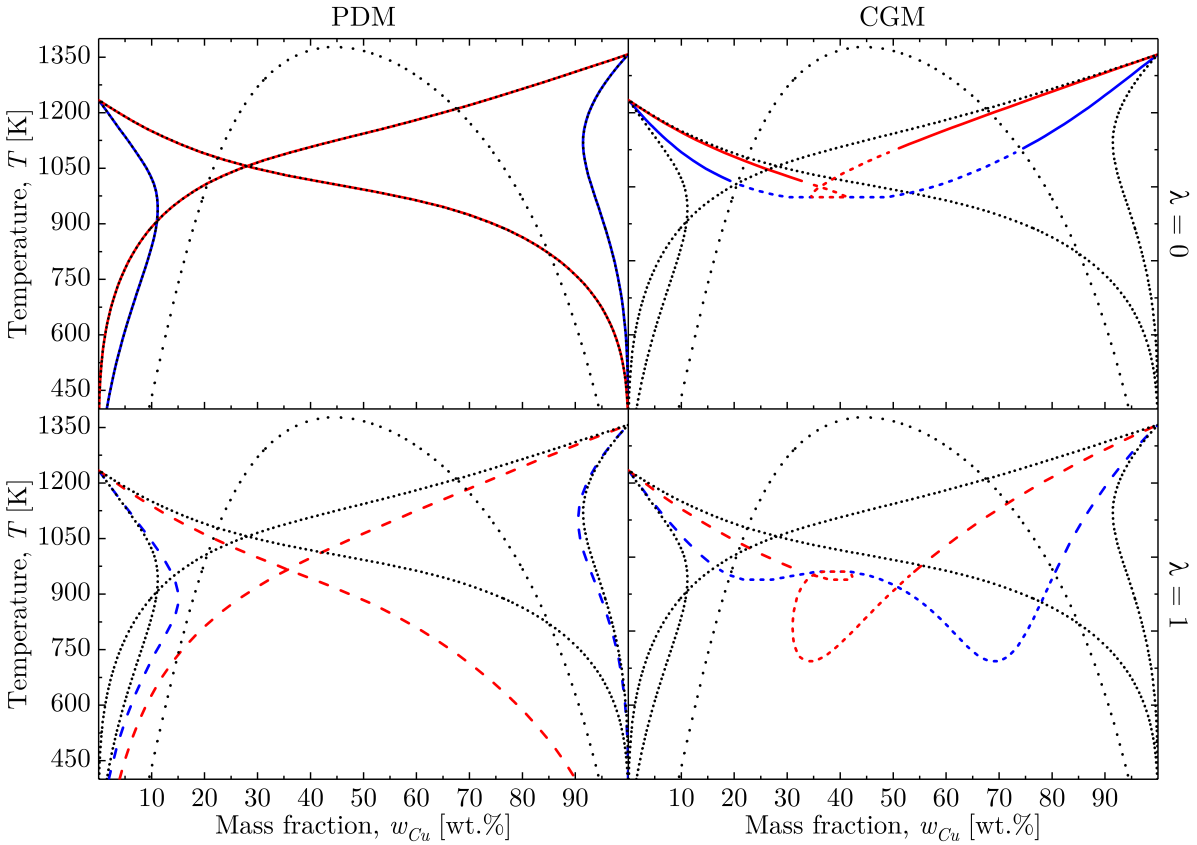

Figure 3: Phase diagram boundaries for the Ag–Cu system (top, plain and short dash) without solute drag ($\lambda = 0$) and (bottom, long and short dash) full solute drag ($\lambda = 1$) for (left) the PDM of Hareland et al. [23] and (right) the CGM of Aziz and Kaplan [3]. Only the stable and metastable solid/liquid boundaries are drawn, with (red) liquidus temperatures, T_L, and (blue) solidus temperatures, T_S, for both the Ag-rich and Cu-rich solids. The equilibrium liquidus temperatures, ${}^eT_L$, and solidus temperatures, ${}^eT_S$, are represented by dotted black curves. The spinodal of the solid phases is shown by the sparsely dotted black curve. Portions of the phase boundaries entering the region of solid spinodal decomposition are represented by short dashed curves. Kinetic parameters: $v = 0.1\,\mathrm{m}\cdot\mathrm{s}^{-1}$, $v^D = 0.4\,\mathrm{m}\cdot\mathrm{s}^{-1}$, and $v_0 = 850\,\mathrm{m}\cdot\mathrm{s}^{-1}$.

Figure 4 shows the Ag-rich part of the phase diagram at various values of the interfacial velocity for an intermediate solute drag parameter, $\lambda = 0.5$. As expected, the liquidus temperature, T_L, decreases monotonically for all compositions as the interfacial velocity increases in both the PDM and the CGM. This is a direct visualization of the kinetic undercooling at these various velocities. Additionally, as the velocity increases, both the kinetic liquidus and solidus converge. As will be shown in Figure 5, this line of convergence is the T_0 line, which itself monotonically decreases with increasing velocity. Because the kinetic solidus approaches the T_0 line from below, neither a monotonic increase or decrease in T_S with v is observed. Additionally, note that the retrograde solidus seen at $v = 0.1\,\mathrm{m}\cdot\mathrm{s}^{-1}$ in the PDM (Figure 3) disappears as v increases to $1\,\mathrm{m}\cdot\mathrm{s}^{-1}$. Although not visible in Figure 4, the CGM still does not capture

the retrograde solidus, even at a velocity of $0.01\,\mathrm{m}\cdot\mathrm{s}^{-1}$, an order of magnitude smaller than that in Figure 3.

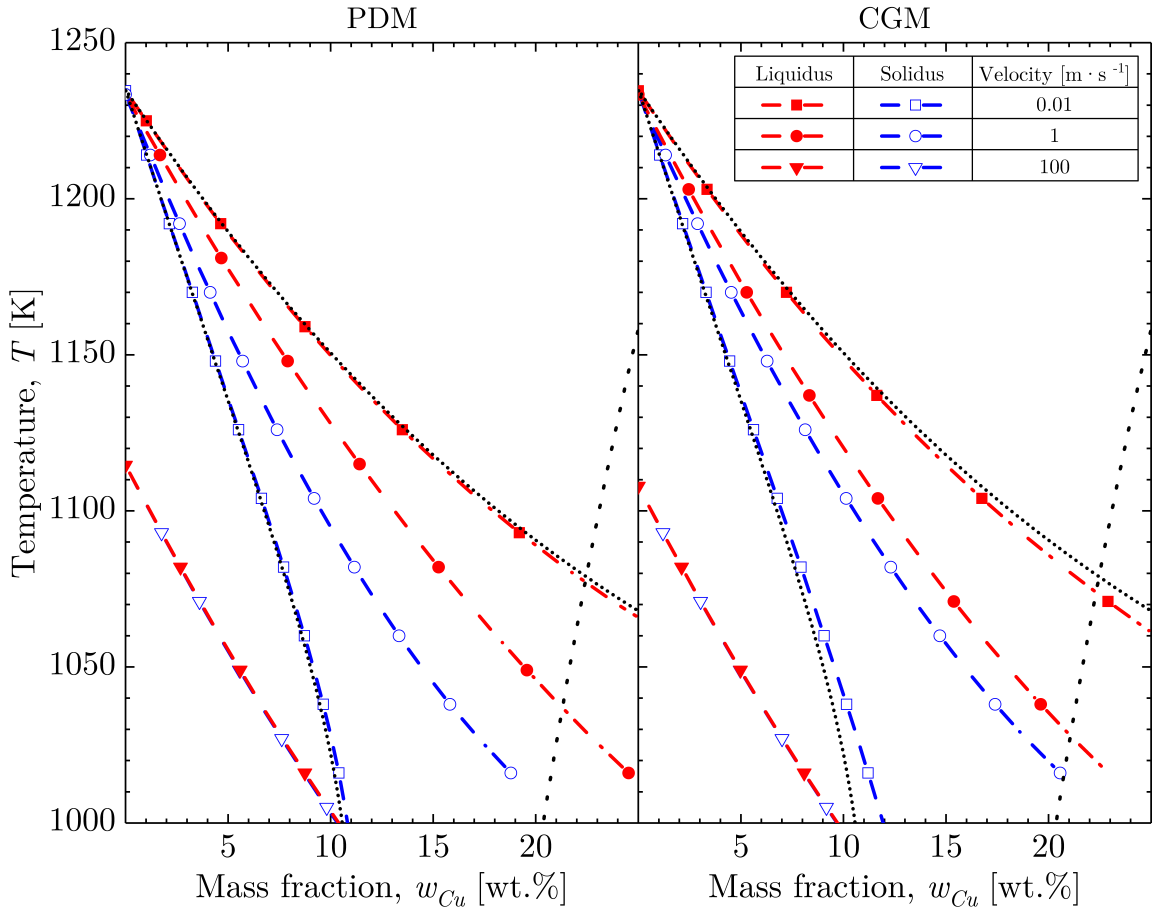

Figure 4: Phase diagram boundaries for the Ag-rich side of the Ag–Cu system computed with (left) the PDM of Hareland et al. [23] and (right) the CGM of Aziz and Boettinger [4] as a function of the velocity, $v \in \{0.01, 1, 100\}$ $[\mathrm{m}\cdot\mathrm{s}^{-1}]$. Curves are (red) the liquidus temperatures, T_L, (blue) the solidus temperatures, T_S, (black dot) the equilibrium liquidus, ${}^eT_L$, and solidus, ${}^eT_S$, temperatures, and (sparse black dot) the spinodal of the solid phases. Kinetic parameters : $\lambda = 0.5$, $v^D = 0.4\,\mathrm{m}\cdot\mathrm{s}^{-1}$, and $v_0 = 850\,\mathrm{m}\cdot\mathrm{s}^{-1}$.

Figure 5 shows the effects of v and λ on the thermodynamic quantities for Ag–5 wt%Cu for both the PDM (top) and CGM (bottom). First, we note that the behavior of the kinetic liquidus and solidus curves reflect the behavior described by Aziz and Boettinger [4]: the liquidus temperature decreases monotonically with increasing v, while the solidus temperature initially rises with increasing v before falling. The solidus curve shows this behavior because the solid composition is fixed at the nominal alloy composition for steady-state plane-front solidification. Initially, as solute trapping increases due to increasing velocity, the partitioning is reduced, causing a decrease in the solutal undercooling and causing the interfacial temperature to rise . However, as velocity continues to increase, the effects of attachment kinetics in the VRF begin to dominate, leading to an overall decrease in the liquidus temperature. The kinetic T_0 curve decreases monotonically with v. As v increases and complete solute trapping (i.e.,

partitionless solidification) is approached, the T_S, T_L, and T_0 curves converge. The effects of partial solute drag, i.e., the value of λ, on T_S, T_L, and T_0 are as follows. In the PDM, the value of T_L is observed to decrease monotonically with increasing λ, while a monotonic decrease of both T_L and T_S with increasing λ is observed in the CGM. However, the behavior of T_S with λ in the PDM is neither a monotonic increase nor decrease, which is a consequence of the coupling between the VRF and CRF due to partial solute drag in this model. Additionally, a rather large discrepancy in interfacial temperatures is observed between the two models for $v \gtrsim 10^{-2}$ m $\cdot$ s^{-1}. This behavior is expected because the CGM requires a trans-interface diffusion speed 3–4 times larger than that in the PDM to predict the same amount of solute trapping [23, 17]. Here, since the value of v^D is the same for both models, the onset of solute trapping begins at lower velocities in the CGM than the PDM. Even in this relatively dilute binary alloy, the effect of partial solute drag can lead to unexpected behaviors and deviations from classical theory when treated self-consistently. Finally, because the T_0 curve is independent of the effects of partial solute drag and relies only on the VRF, it is identical between the two models over the range of velocities shown here, i.e. for $v/v_0 \ll 1$ so that the VRF equations for the CGM and PDM models reported in Table A.1 are equivalent.

The behavior of the T_S and T_L curves in the zero-drag case ($\lambda = 0$) of the PDM is also worth mentioning. It corresponds to the limit in which material can always solidify at the composition of the solid (i.e., $\lambda = 0 \implies x_i^{eff} = x_i^{sl}$). Thus, $\Delta G^t = 0$, so all the energy is dissipated by interface motion in the VRF and the solidus temperature only begins to decrease when the effects of interfacial attachment kinetics become significant. Because the trans-interface flux of the CGM does not account for partial solute drag, this effect is not observed in the CGM. However, as soon as any amount of solute drag is added, the aforementioned increase in solidus temperature with velocity is observed as the effect of trans-interface diffusion becomes active. Additionally, the width of the two-phase region, i.e., the difference between T_L and T_S, remains nearly constant in the PDM for the entire range of velocities, reflecting a partition coefficient that also remains nearly constant with velocity. Hence, without solute drag, no solute trapping is predicted by the PDM.

3.2. Dendrite tip kinetics

Figure 6 displays various quantities from the calculations of dendrite tip kinetics for the Ag–5 wt% Cu alloy, using the PDM [23] with $\lambda = 0.5$ and the parameters listed in Table 2. Figure 6a shows the dendrite tip temperature alongside the planar solidus, liquidus, and T_0 curves. The latter three curves show the same behavior as observed in Figure 5. For $v < 10^{-1}$ m $\cdot$ s^{-1}, the dendrite tip temperature (black, T_d) is only slightly lower the equilibrium dendrite tip temperature (dotted black, ${}^eT_d$) due to a minor contribution from kinetic effects at these velocities, and then merges smoothly into the kinetic solidus curve at the absolute stability limit. Figure 6b shows the tip radius of the dendrite as a function of velocity. The primary difference between the equilibrium dendrite tip (dotted black) and the non-equilibrium dendrite tip (dash-dotted black) is the value of the absolute stability limit, which is nearly an order of magnitude lower in the non-equilibrium case, even for this relatively dilute alloy. This behavior is consistent with the original simulation results for Ag–Cu alloys [5]. However, models of dendritic growth using the marginal stability criterion, even for the case of zero solute drag, have been known to

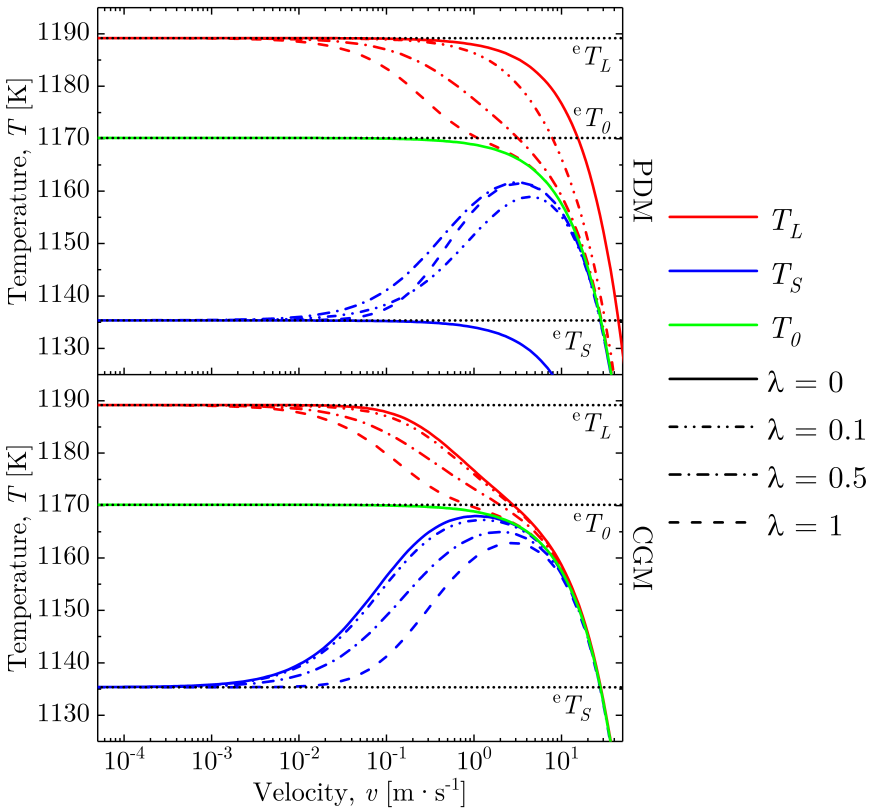

Figure 5: Velocity-dependent (red) liquidus temperature, T_L, (blue) solidus temperature, T_S, and (green) T_0 temperature, (grey dot) the equilibrium liquidus temperature, ${}^eT_L$, and equilibrium solidus temperatures, ${}^eT_S$ and the ${}^eT_0$ temperature for the Ag–5 wt% Cu alloy with (top) the PDM of Hareland et al. [23] and (bottom) the CGM of Aziz and Boettinger [4]. Kinetic parameters : $\lambda \in \{0,\ 0.1,\ 0.5,\ 1\}$, $v^D = 0.4\,\mathrm{m}\cdot\mathrm{s}^{-1}$ and $v_0 = 850\,\mathrm{m}\cdot\mathrm{s}^{-1}$.

underpredict the experimentally observed limit of absolute stability [50], so using the solvability condition as described earlier may be necessary in order to obtain agreement with experiment. Figure 6c shows the composition in the liquid at the dendrite tip as a function of velocity. Notably, including kinetic effects (dash-dotted black) begins to decrease the composition above $v \approx 0.3\,\mathrm{m}\cdot\mathrm{s}^{-1}$ from the equilibrium result (dotted black) as the effect of solute trapping starts to become significant. Finally, Figure 6d shows the various contributions to the total undercooling described by Eqs. (16) – (19). In this case, the solutal undercooling, ΔT_χ, completely dominates the total undercooling at low velocities, and is the most significant contribution at all velocities in the window of dendritic growth. The behavior of the solutal undercooling curve reflects that of Figure 6c, that is, a decrease around $v \approx 0.2\,\mathrm{m}\cdot\mathrm{s}^{-1}$ as solute partitioning decreases due to the onset of solute trapping. The curvature undercooling, ΔT_κ, mirrors the behavior in Figure 6b, reflecting a curvature undercooling inversely proportional to the tip radius. Finally, as expected, the kinetic undercooling, ΔT_v, is negligible at low velocities, but increases monotonically with velocity.

The effect of solute drag on the interfacial temperatures is shown in Figure 7. The interfacial temperatures in the zero-drag and full-drag limits of both the PDM and CGM are shown for the parameters

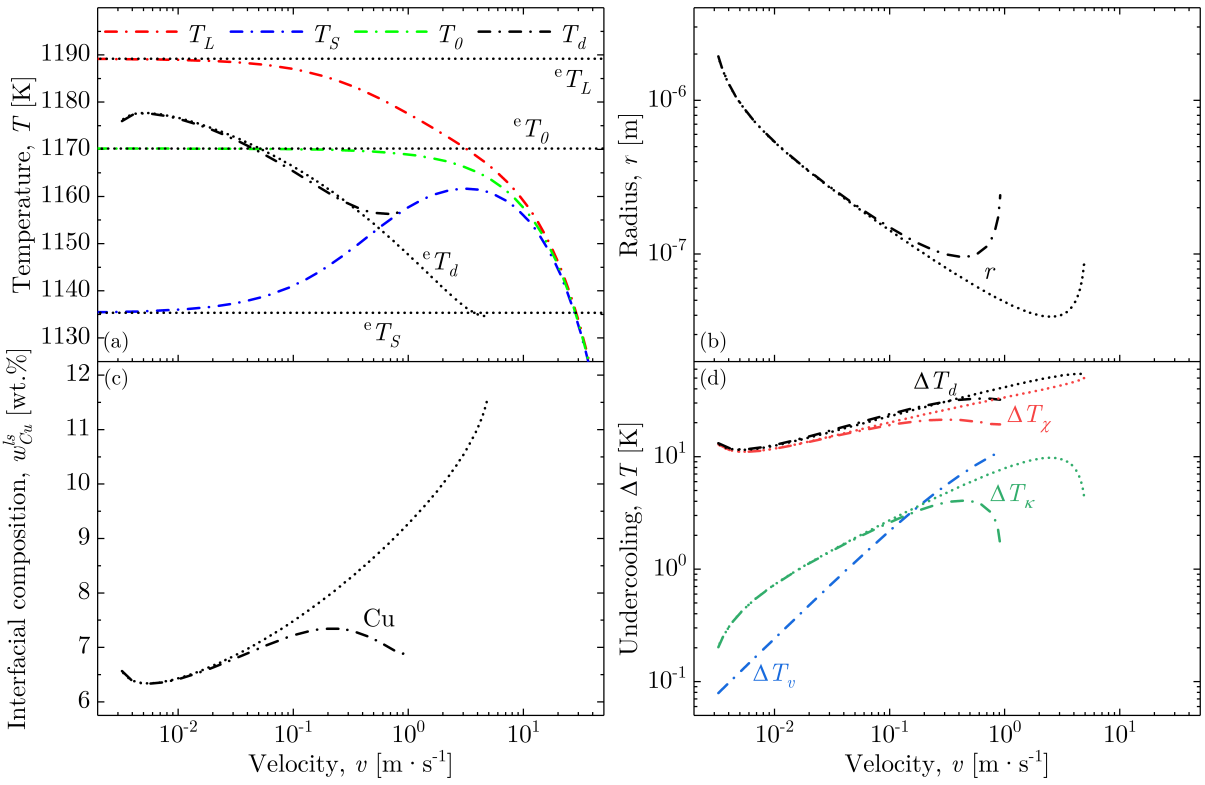

Figure 6: Dendrite tip kinetics for a Ag–5 wt% Cu alloy with (a) tip temperature, T_d, (b) tip radius, r, (c) tip composition in the liquid, w^{ls}_{Cu}, (d) total tip undercooling, ΔT_d, summation of the contributions due to curvature, ΔT_κ, solute diffusion, ΔT_χ, and non-equilibrium effects, ΔT_v, using the PDM model of Hareland *et al.* [23]. Kinetic parameters : $\lambda = 0.5$, $v^D = 0.4\,\mathrm{m \cdot s^{-1}}$ and $v_0 = 850\,\mathrm{m \cdot s^{-1}}$. The calculation assuming thermodynamic equilibrium at the solid-liquid interface [24] is displayed as dotted curves for comparison, labelled with superscript ${}^e\{.\}$, (a-c) in black and (d) in color.

listed in Table 2. The behavior of the planar interface, i.e., the T_S, T_L, and T_0 curves, is analogous to that seen in Figure 5. Figure 7a shows the zero-drag case of the PDM. As before, because the CRF of the PDM incorporates partial solute drag, deviations from the equilibrium case (i.e., kinetic undercooling) only occur at large velocities, as the only active kinetic effect in this limit is that of interfacial attachment kinetics. Note that the dendrite tip temperature dips slightly below the solidus temperature near the absolute stability limit due to the effects of interfacial curvature. Interestingly, the zero-drag limit of the CGM (Figure 7b) predicts an increase in dendrite tip temperature from the equilibrium case. This is rather counterintuitive, as the kinetic effects are expected to reduce the driving force available for interface motion, lowering the interfacial temperature at a given velocity. Here, the active kinetic effects are both attachment kinetics due to v_0 and solute trapping due to the absence of λ in the CRF of the CGM. The full-drag cases of both models (Figure 7c and 7d) reflect the expected behavior: a decrease in dendrite tip temperature due to the effect of solute drag dissipating energy that would otherwise be used to advance the interface. Additionally, note that the change in the absolute stability limit between the zero-drag and full-drag cases of the CGM is very small, while the decrease in the absolute stability limit when moving from the zero-drag to the full-drag case is nearly an order of magnitude in the PDM;

the same trend is observed in Figure 6b.

It is also interesting to note that the value of λ affects the rate at which T_L and T_S approach T_0 with increasing velocity, which implies that the kinetic liquidus and solidus are not necessarily centered around the T_0 line. As $\lambda \to 1$, the kinetic liquidus meets the T_0 line at a lower velocity than the solidus. Conversely, as $\lambda \to 0$, the kinetic solidus meets the T_0 line at a lower velocity than the liquidus. For values of $\lambda \approx 1/2$, as in Figure 6a, the kinetic liquidus and solidus will converge to the T_0 line at approximately the same velocity. This behavior is a consequence of solute trapping—as the solidification velocity increases, the system tends towards complete solute trapping, so the behavior of CRF becomes increasingly negligible relative to the VRF and the system of interfacial response functions increasingly resembles the single T_0 equation. If the velocity is sufficiently high such that the contribution of the CRF is negligible, the VRF with $\lambda \to 0$ (i.e., $x_i^{eff} \to x_i^{sl}$) recovers the T_0 equation with $\mathbf{x^0} = \mathbf{x^{sl}}$, and the VRF with $\lambda \to 1$ (i.e., $x_i^{eff} \to x_i^{ls}$) recovers the T_0 equation with $\mathbf{x^0} = \mathbf{x^{ls}}$. Thus, the value of the solute-drag parameter affects the relative rates at which the kinetic phase boundaries approach the T_0 line.

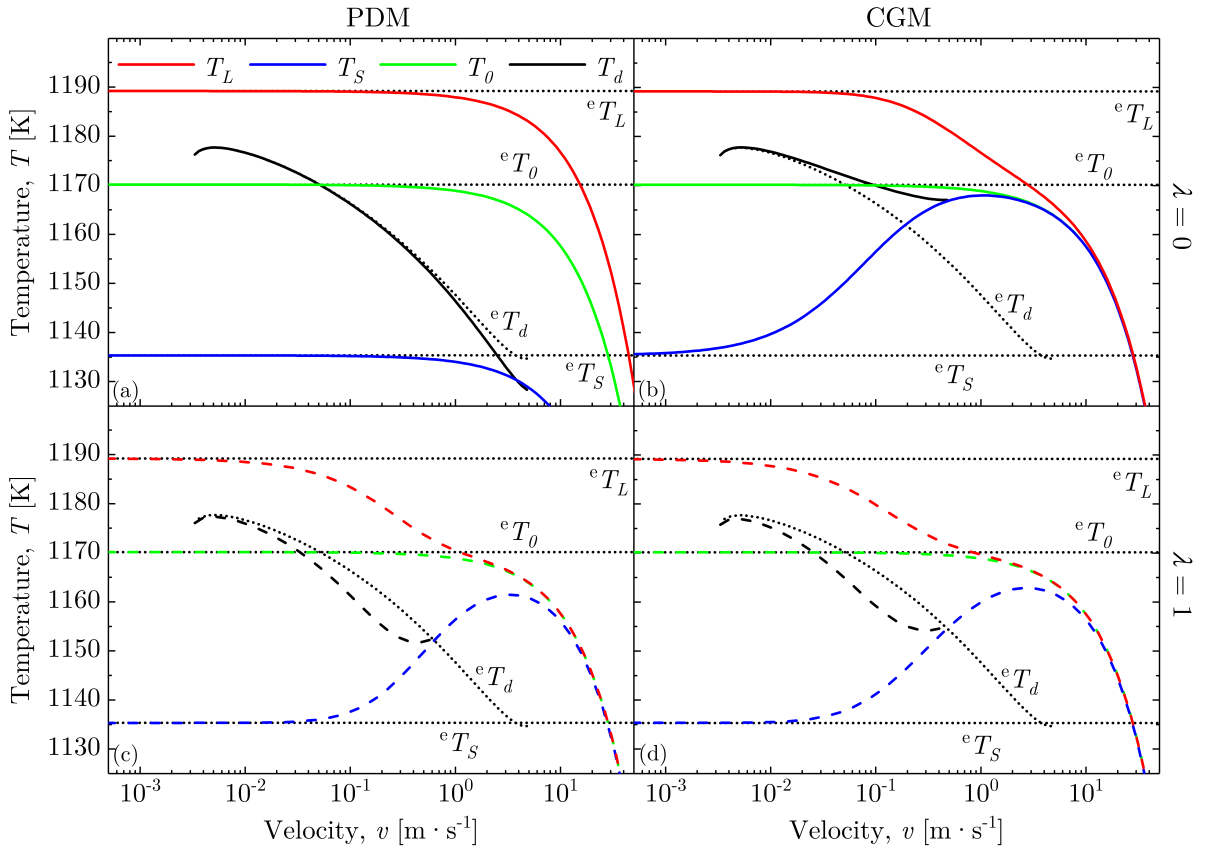

Figure 7: Dendrite tip temperature, T_d, for the Ag–5 wt% Cu alloy with non-equilibrium kinetics using (a, c) the PDM model of Hareland *et al.* [23] and (b, d) the CGM model of Aziz and Kaplan [3] with parameters (a, b) no solute drag, $\lambda = 0$, and (c, d) full solute drag, $\lambda = 1$. Kinetic parameters: $v^D = 0.4\,\mathrm{m \cdot s^{-1}}$ and $v_0 = 850\,\mathrm{m \cdot s^{-1}}$. The calculation assuming thermodynamic equilibrium at the solid-liquid interface [24] is displayed as dotted grey curves for comparison, labelled with superscript $^e\{.\}$.

4. Application to multicomponent alloys

In this section, the present model is applied to multicomponent alloys of industrial interest. The main advantages compared to usual pseudo-binary methodologies encountered in the literature are shortly summarized hereafter:

- *Coupling with CALPHAD thermodynamic databases* provides a full description of the multicomponent tie lines from assessed thermodynamic properties [25, 51], avoiding the need to directly compute segregation coefficients and liquidus slopes, and/or use linear phase diagrams where the effects of individual solute elements are superimposed.

- *Coupling with CALPHAD mobility databases* [26, 52] provides the full diffusion matrix in the liquid phase, avoiding the need to define an equivalent diffusion coefficient [53]. This is enabled by integrating the multicomponent dendrite tip theory developed by Hunziker [27].

- *Direct computation of the Gibbs-Thomson effect* is achieved by adding the excess Gibbs free energy due to curvature to the chemical potential of the solid phase. This allows the effects of curvature on the temperature and composition in both the solid dendrite tip and the liquid phase to be incorporated directly in the calculation instead of relying on the addition of the typical curvature undercooling term, $\Delta T_\kappa = 2\Gamma/r$.

- *Direct computation of the non-equilibrium phase boundaries* [23], as demonstrated above, allows the velocity-dependent liquidus temperature, solidus temperature, and T_0 temperature to be computed directly. This eliminates the need for the typical approximations developed for binary dilute-ideal solutions [2, 3, 4] yet commonly applied to non-dilute alloys.

- *Accounting for partial solute drag* improves the estimates of the constitutive kinetic parameters (i.e., λ, v_0, and v_i^D) in the computation of the non-equilibrium phase boundaries, which can be obtained directly from atomistic simulations and physically represent interfacial behavior when partial solute drag is considered [17]. Although there are only a few such studies for binary alloys [14, 15, 16, 17], and (to the best of the authors' knowledge) none for multicomponent systems, the existing results for binary alloys provide a much better approximation of the kinetic coefficients than the typical order-of-magnitude estimates. Here, as a first approximation, we use values of v_i^D obtained from atomistic simulations of relevant binary systems, and assume the value of v_i^D is the same for each solute species.

4.1. Application to Inconel 718

IN718 is an industrial Ni-base superalloy used in many different solidification-based processes to produce components for a variety of high-temperature applications. The composition and the relevant material parameters are reported in Table 3 and in Table 4, respectively. The kinetic parameters v_0 and v_i^D are taken from Ref. [23], in which the MD study of the rapid solidification behavior of Ni–Cu by Yang et al. [14] is fit with the interface response functions used herein, thus accounting for the effects of

Chemical elements	Cr	Fe	Nb	Mo	Ti	Al	C	Ni
Nominal composition, w_i^0 [wt%]	18.2	18.9	5.1	3.1	0.9	0.29	0.025	Balance
Liquidus slope, ${}^e m_i^{ls}$ [K·wt%$^{-1}$]	-2.65	-0.74	-9.57	-4.34	-18.16	-10.25	-44.98	
Segregation coefficient, ${}^e k_i^{s/l}$ [wt·wt^{-1}]	1.03	1.12	0.39	0.71	0.46	0.97	0.10	
Nominal composition x_i^0 [mol%]	20.37	19.69	3.19	1.88	1.09	0.63	0.12	Balance
Liquidus slope, ${}^e m_i^{ls}$ [K·mol%$^{-1}$]	-2.53	-0.78	-14.42	-6.23	-15.22	-5.54	-10.45	
Segregation coefficient, ${}^e k_i^{s/l}$ [mol·mol^{-1}]	1.02	1.10	0.38	0.70	0.46	0.96	0.10	

Table 3: Chemical composition and phase diagram properties at the equilibrium liquidus temperature, ${}^e T_L = 1613.3\,\mathrm{K}$ for alloy IN718 [54, 25]

Property	Symbol	Value	Unit	Ref
Thermodynamic database		TCNI10		[25]
Solute-drag parameter	λ	0., 0.1, 0.5, 1.	$[\mathrm{mol \cdot mol^{-1}}]$	
Maximum crystallisation speed	v_0	850	$[\mathrm{m \cdot s^{-1}}]$	[23]
Trans-interface diffusion speed	v_i^D	0.4	$[\mathrm{m \cdot s^{-1}}]$	[23]
Mobility database		MOBNI5		[26]
Equilibrium liquidus temperature	${}^e T_L$	1613.3	[K]	[25]
Diffusion matrix in liquid at ${}^e T_L$	$\mathbf{D}$	–	$[\mathrm{m^2 \cdot s^{-1}}]$	[24]
Interfacial energy	γ	0.37	$[\mathrm{J \cdot m^{-2}}]$	[24]
Selection parameter	σ	$(2\pi)^{-2}$	[–]	[5]
Temperature gradient	G	10^4	$[\mathrm{K \cdot m^{-1}}]$	[5]

Table 4: Material parameters for IN718.

partial solute drag. Due to the scarcity of such MD studies, this is the best available estimate of these parameters.

Figure 8 shows the interfacial temperature as a function of velocity for various values of the solute-drag parameter using the multicomponent equations of both the PDM and CGM. The behaviors are qualitatively identical to those observed in the binary case (Figure 5): the CGM displays a monotonic decrease in T_L, T_S, and T_0 with λ, while the PDM displays a monotonic decrease in T_L and T_0 with λ and non-monotonic behavior of T_S as described in Section 3.1. Additionally, the evolution of the kinetic solidus and liquidus towards the T_0 line reflects the λ-dependence described in Section 3.2.

Figure 9 shows the interfacial conditions at the dendrite tip as a function of velocity using the PDM with $\lambda = 0.5$. The observed behavior in (a)–(d) is qualitatively identical to that in Figure 6. Figure 9e shows the partition coefficients for each element computed at the dendrite tip (solid curves), the non-equilibrium liquidus temperature (dashed curves), and the non-equilibrium solidus temperature (dotted curves). Due to the relatively low temperature gradient and the non-linear phase diagram, the partition coefficient for each solute at the dendrite tip begins near the value at the liquidus temperature at low velocity and evolves smoothly to end at the value at the non-equilibrium solidus temperature at high velocity. This behavior mirrors the evolution of the tip temperature from Figure 9a. Additionally,

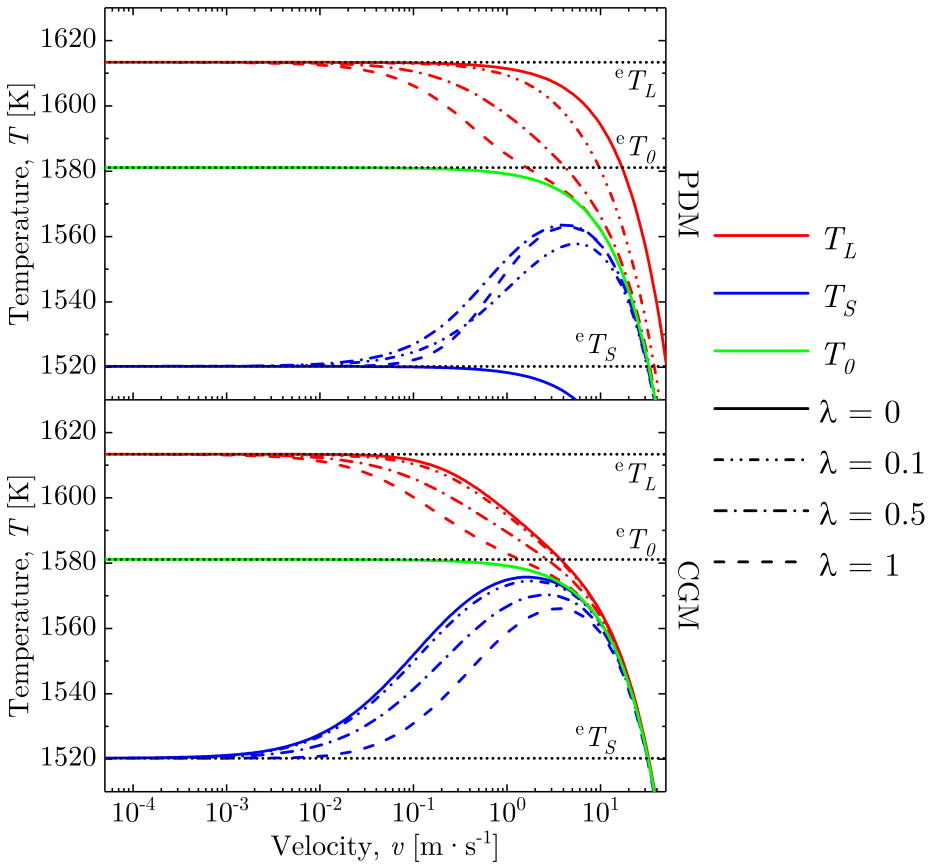

Figure 8: Velocity-dependent (red) liquidus temperature, T_L, (blue) solidus temperature, T_S, and (green) T_0 temperature, (dotted grey) the equilibrium liquidus temperature, ${}^{e}T_L$, and equilibrium solidus temperatures, ${}^{e}T_S$ and the ${}^{e}T_0$ temperature for the IN718 alloy with (top) the PDM of Hareland et al. [23] and (bottom) the CGM of Du et al. [29]. Kinetic parameters : $\lambda \in \{0,\ 0.1,\ 0.5,\ 1\}$, $v_i^D = 0.4\,\mathrm{m \cdot s^{-1}}$, and $v_0 = 850\,\mathrm{m \cdot s^{-1}}$.

all partition coefficients smoothly evolve towards unity as the velocity increases and complete solute trapping is approached. Due to the combined effects of non-linear phase boundaries and solute trapping, the evolution of partition coefficients at the dendrite tip can be highly non-monotonic. For example, k_{Al} computed at the dendrite tip (solid orange curve) is less than unity at low velocities, i.e. very close to the value computed at the liquidus temperature (dashed orange curve). It increases monotonically as the velocity increases and the dendrite tip temperature evolves towards the kinetic solidus temperature, hence catching up with the k_{Al} curve computed at the solidus temperature (dotted orange curve). At velocities higher than $\approx 0.1\,\mathrm{m \cdot s^{-1}}$, k_{Al} begins to decrease as the kinetic effects become significant. These observations are the results of both the non-linearity of the phase diagram and the kinetic effects. Additionally, while the partition coefficients spanning the two-phase regions for all other elements are either entirely above or below unity, the range for Al is relatively very large and spans values ranging from approximately $0.95 \leq k_{Al} \leq 1.6$. Finally, Figure 9f shows the liquidus slopes for each element computed at the dendrite tip (solid curves), the non-equilibrium liquidus temperature (dashed curves), and the non-equilibrium solidus temperature (dotted curves). Qualitatively similar trends are observed

for the liquidus slopes at the dendrite tip as for the partition coefficients at the dendrite tip in Figure 9e; they begin at values close to those at the liquidus temperatures and evolve smoothly towards values at the solidus temperatures as velocity increases. As with the partition coefficients, the evolution of the liquidus slopes can be highly non-monotonic due to the combination of non-linear phase boundaries and kinetic effects (e.g., C). It is interesting to note from Figure 9e and 9f that $m_i^{ls} < 0$ for all elements, while the values of $k_i^{s/l}$ are both above and below unity. While solidification in binary alloys requires either $k^{s/l} < 1$ and $m^{ls} < 0$ or $k^{s/l} > 1$ and $m^{ls} > 0$, multicomponent alloys can deviate from this behavior [55], as is observed here.

In Figure 10, we revisit the velocity/undercooling power law for IN718 that was presented with the full multicomponent kinetic theory assuming (dotted) interface equilibrium, ${}^{e}\Delta T_d$, and (solid red) the CGM approximation, $\overline{\text{CGM}}\Delta T_d$, established for an ideal dilute alloy with zero solute drag [24]. The figure also includes the (red) predictions for $\overline{\text{CGM}}\Delta T_d$ with (dashed dotted) partial solute drag $\lambda = 0.5$ and (dashed) full solute drag $\lambda = 1$ using the classical formulation for the kinetic liquidus slope [4]:

$$m_i^{ls} = {}^{e}m_i^{ls}\,\frac{1 - k_i^{s/l} + \left[k_i^{s/l} + \lambda\,\left(1 - k_i^{s/l}\right)\right]\ln\left(k_i^{s/l}/{}^{e}k_i^{s/l}\right)}{1 - {}^{e}k_i^{s/l}} \tag{20}$$

The three blue curves show the CGM solution coupled with CALPHAD data [29], ${}^{\text{CGM}}\Delta T_d$, again with full solute drag $\lambda = 1$, zero-solute drag $\lambda = 0$, and partial solute drag $\lambda = 0.5$. Finally, the curves deduced from using the present model with the PDM, ΔT_d, are shown in black. The data corresponding to the (dashed dotted) PDM $\lambda = 0.5$ and (dotted) interface equilibrium curves are the same as in Figure 9d. Detailed explanations of the methodology to compute the total undercooling with the CGM approximation established for an ideal-dilute alloy is provided in Reference [24], and data for the equilibrium values using the TCNI10 thermodynamic database are reported in Table 3. Note that, for comparison with the present simulations, values of parameters v_0 and v_i^D are the same as in Figure 9, also reported in Table 4, and hence differ from the values in Reference [24]. All other values of the parameters, i.e. the computed Gibbs-Thomson coefficient, $\Gamma = 3.355 \cdot 10^{-7}\ \text{K} \cdot \text{m}$, the entropy of fusion, $\Delta S_f = 9.1016\ \text{J} \cdot \text{mol}^{-1} \cdot \text{K}^{-1}$, and the diffusion matrix are the same as in Reference [24]. A first observation when comparing the curves is that, for a given value of the solute-drag parameter, the ranges of undercooling and velocity progressively increase when going from the $\overline{\text{CGM}}\Delta T_d$ to ${}^{\text{CGM}}\Delta T_d$ to ΔT_d. This means that the absolute stability limit for dendritic growth is reached at a lower velocity and a lower undercooling with the CGM model than with the PDM, and the minimum values are obtained when using the ideal-dilute alloy approximations. It is also clear that all the curves remain almost superimposed up to approximately 35 K, reflecting the absence of non-equilibrium effects for velocities lower than $\sim 0.1\,\text{m} \cdot \text{s}^{-1}$, and implying that a velocity/undercooling power law determined under the assumption of interface equilibrium remains valid for low undercoolings. Additionally, in the PDM, increasing λ causes the kinetic curve to depart from the equilibrium curve at lower velocities as the effect of solute drag becomes more significant. The non-linear evolution of the solidus temperature with λ for the PDM, reported and discussed in Figure 8, is retrieved here; the undercooling reached at the velocity of the absolute stability limit decreases from $\lambda = 0$ to $\lambda = 0.5$ and then increases from $\lambda = 0.5$ to $\lambda = 1$. The expected trends for the CGM are retrieved as well with maximum undercooling and velocity increasing with λ. The same behaviors are

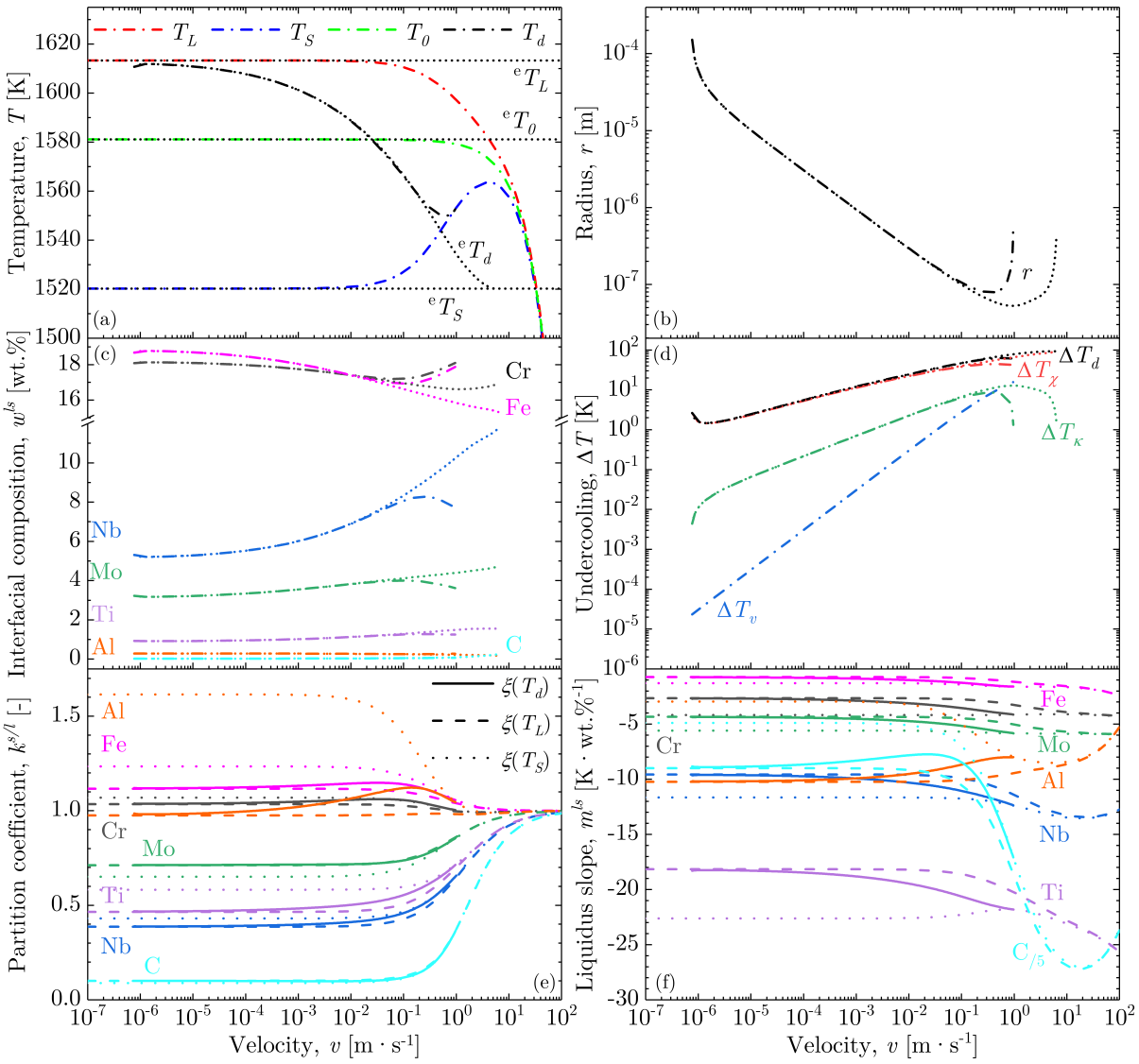

Figure 9: Dendrite tip kinetics for the IN718 alloy with (a) tip temperature, T_d, (b) tip radius, r, (c) tip composition in the liquid, w^{ls}, (d) total tip undercooling, ΔT_d, summation of the contributions due to curvature, ΔT_κ, solute diffusion, ΔT_χ, and non-equilibrium effects, ΔT_v, (e) segregation coefficient, $k^{s/l}$ [wt%·wt%$^{-1}$], and (f) liquidus slope, m^{ls}. The PDM model [23] is considered with kinetic parameters: $\lambda = 0.5$, $v^D = 0.4\,\mathrm{m \cdot s^{-1}}$ and $v_0 = 850\,\mathrm{m \cdot s^{-1}}$. The calculation assuming thermodynamic equilibrium at the solid-liquid interface [24] is displayed as dotted curves for comparison, labelled with superscript ${}^e\{.\}$. Note that the liquidus slope of C in (f) is divided by 5 for the sake of visualization. In (e) and (f), quantities are plotted (dashed) at the liquidus temperature, (dotted) at the solidus temperature and (solid) at the dendrite tip temperature.

present for the Ag–5 wt% Cu alloy in Figure 5.

4.2. Application to 316L stainless steel

The various solidification paths observed during the welding of steels [56, 57, 58] have recently attracted much interest due to a wide range of experimental observations of the primary solidification mode

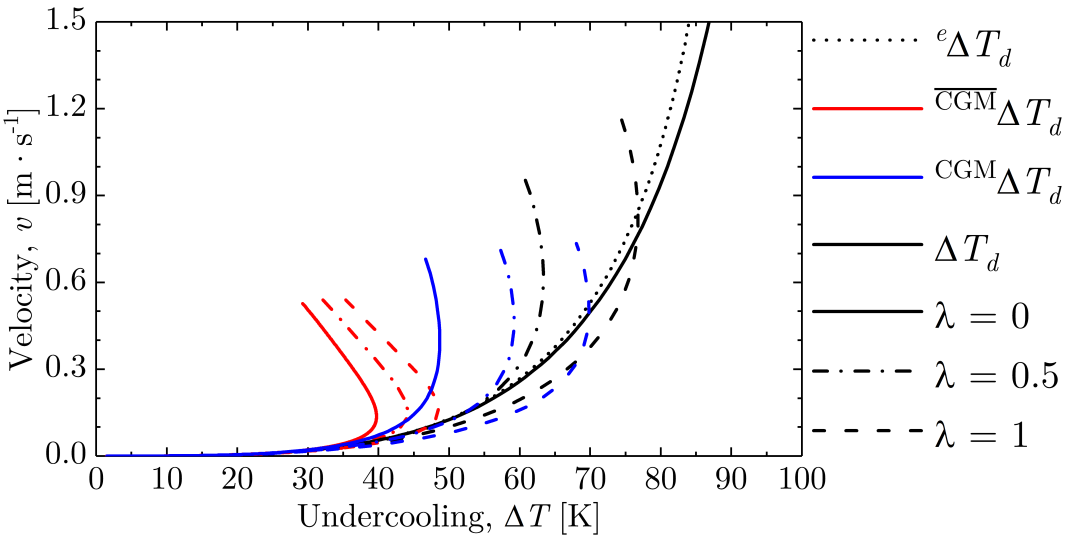

Figure 10: Dendrite tip velocity as a function of the total undercooling for the IN718 alloy comparing (solid) zero-drag $\lambda = 0$, (dashed dotted) partial drag $\lambda = 0.5$ and (dashed) full-drag $\lambda = 1$ solutions using (black) the present PDM model [23], ΔT_d, (blue) the CGM model, $^{\mathrm{CGM}}\Delta T_d$, and (red) the CGM approximation established for an ideal dilute alloy [4, 24], $\overline{^{\mathrm{CGM}}}\Delta T_d$. Solutions ΔT_d and $^{\mathrm{CGM}}\Delta T_d$ are fully coupled with CALPHAD. The local equilibrium dendrite tip model [24], $^{e}\Delta T_d$, is added (dotted). Both $^{e}\Delta T_d$ and $\Delta T_d(\lambda = 0.5)$ are extracted from Figure 9.

during AM [59, 60, 61, 53, 62]. Hereafter, we focus on the reported results by Godfrey et al. for 316L [53], which considered the origin of the so-called "fish-scale" structure formed at the boundaries of the melt pool during AM using laser powder-bed fusion. Their interpretation suggests that this structure results from the competition between primary $\delta-$ferrite dendrites and primary $\gamma-$austenite dendrites formed from the melt and relies on a model of dendritic growth incorporating interfacial response functions to calculate the velocity/temperature relationships for both $\delta-$ferrite and $\gamma-$austenite dendrites. In light of the shortcomings of their dendrite tip model, summarized at the beginning of Section 4, we revisit the results with the present multicomponent theory.

Chemical element	Cr	Ni	Mo	Mn	Si	Fe
Nominal composition, w_i^0 [wt%]	16.81	11.92	2.43	0.99	0.36	Balance

Table 5: Chemical composition of the 316L in Ref. [53] considered here.

The composition of 316L in the Gulliver–Scheil calculations of Ref. [53] and examined herein is listed in Tab. 5. The minor elements (0.08 Co – 0.05 O – 0.01 N – 0.005 P – 0.001 C) reported in Ref. [53] are omitted. The kinetic parameters are taken from the study of the binary Fe–Cr system by Antillon et al. [17] because atomistic simulations of solute trapping have not been performed for multicomponent stainless steels. The temperature field is estimated from a heat flow simulation [53], and the authors report temperature gradients and isotherm velocities between $[10^6, 10^8]$ K · m^{-1} and $[10^{-2}, 1]$ m · s^{-1}, respectively. For the transport of the chemical species in the liquid, the full diffusion matrix is extracted from the CALPHAD databases TCFE10 [51] and MOBFE5 [52] at the equilibrium liquidus temperature

Property	Symbol	Value		Unit	Ref
		$\delta-$ferrite	$\gamma-$austenite		
Thermodynamic database		TCFE10			[51]
Solute-drag parameter	λ	0.58	0.52	$[\mathrm{mol}\cdot\mathrm{mol}^{-1}]$	[17]
Maximum crystallisation speed	v_0	759	614	$[\mathrm{m}\cdot\mathrm{s}^{-1}]$	[17]
Trans-interface diffusion speed	v_i^D	0.72	0.36	$[\mathrm{m}\cdot\mathrm{s}^{-1}]$	[17]
Mobility database		MOBFE5			[52]
Equilibrium liquidus temperature	${}^{\mathrm{e}}T_L$	1725.9	1714.3	[K]	[51]
Diffusion matrix in liquid at ${}^{\mathrm{e}}T_L$	$\mathbf{D}$	$-$		$[\mathrm{m}^2\cdot\mathrm{s}^{-1}]$	[51, 52]
Interfacial energy	γ	0.27		$[\mathrm{J}\cdot\mathrm{m}^{-2}]$	[49]
Selection parameter	σ	$(2\pi)^{-2}$		$[-]$	[5]
Temperature gradient	G	$10^6 - 10^9$		$[\mathrm{K}\cdot\mathrm{m}^{-1}]$	[53]

Table 6: Material parameters for the 316L stainless steel phases $\delta-$ferrite and γ-austenite, respectively referred to as BCC_A2 and FCC_A1 in the CALPHAD databases TCFE10 [51] and MOBFE5 [52].

for $\delta-$ferrite and $\gamma-$austenite (BCC_A2 and FCC_A1 in the databases, respectively). The equilibrium liquidus temperatures for both phases are reported in Table 6. The 5×5 terms of each diffusion matrix are easily computed with Thermo-Calc software [63]. Because the composition of the liquid is the same for the two diffusion matrices and the difference between the equilibrium liquidus for $\delta-$ferrite and $\gamma-$austenite is only 11.6 K, little difference is exhibited between the terms of the two diffusion matrices. Extremum values on the diagonal for BCC are $D_{\mathrm{MoMo}} = 2.6\cdot10^{-9}\ \mathrm{m}^2\cdot\mathrm{s}^{-1}$ and $D_{\mathrm{MnMn}} = 3.8\cdot10^{-9}\ \mathrm{m}^2\cdot\mathrm{s}^{-1}$, with off-diagonal terms in the range $[-3.2\cdot10^{-9}, 6.7\cdot10^{-10}]\ \mathrm{m}^2\cdot\mathrm{s}^{-1}$, demonstrating that interdiffusion for some solute species is of the same order of magnitude as self-diffusion. The other relevant material properties are the energy of the solid/liquid interface, γ, and the dendrite tip selection parameter, σ; the same values of these parameters are used for both the $\delta-$ferrite and $\gamma-$austenite phases, as summarized in Table 6.

Figure 11a shows the liquidus (dashed), solidus (dotted), and dendrite tip (solid) temperatures for the $\delta-$ferrite (red) and $\gamma-$austenite (black) structures. The predictions give a transition from primary $\delta-$ferrite dendrites to primary $\gamma-$austenite dendrites at around $v \approx 3\cdot10^{-2}\ \mathrm{m}\cdot\mathrm{s}^{-1}$, which is well within the range reported for the liquidus isotherm velocity at the edges of the melt pool [53]. The dendrite tip radius for both structures is drawn in Figure 11b as a function of velocity. A difference in length scale can be expected given the difference in tip radii; the $\gamma-$austenite dendrites are predicted to be larger than $\delta-$ferrite dendrites at a given velocity. This is indeed reported by measurements of "dendrite arm spacing of 1 µm or below" for $\gamma-$austenite and "0.5 µm or below" for $\delta-$ferrite in Ref. [53]. Figures 11c and 11d show the partition coefficients calculated for the $\delta-$ferrite and $\gamma-$austenite structures, respectively, at the liquidus temperature (dashed), solidus temperature (dotted), and dendrite tip temperature (solid). As observed for IN718 in Figure 9, the partition coefficients at the dendrite tip at low velocity lie between the equilibrium values at the liquidus and solidus temperatures due to the non-linear phase diagram. As before (as in Figure 9), all the partition coefficients are predicted to smoothly evolve towards unity as

the velocity increases and the system approaches complete solute trapping, and the partitioning of solute species at the dendrite tip (solid) progressively evolves from values close to the non-equilibrium liquidus temperatures (dashed) at low velocity to the values at the non-equilibrium solidus temperatures (dotted) when reaching the stability limit at high velocity, i.e., plane-front solidification. It is worth noting that partitionless solidification is only predicted to occur for plane-front solidification at very high velocities (around $50\,\mathrm{m}\cdot\mathrm{s}^{-1}$). The effects of solute trapping are relatively minor at the absolute stability limits for dendritic growth, which are approximately $0.3\,\mathrm{m}\cdot\mathrm{s}^{-1}$ for $\delta-$ferrite and $0.1\,\mathrm{m}\cdot\mathrm{s}^{-1}$ for $\gamma-$austenite. Figure 11c indicates interdendritic segregation of Ni in the ferritic structure ($k_{Ni}^{\delta/l} \leq 1$) while Figure 11d indicates interdendritic segregation of Mo and Cr in the austenitic structure ($k_{Mo}^{\gamma/l} \leq 1$ and $k_{Cr}^{\gamma/l} \leq 1$). The same behavior was observed via energy-dispersive X-ray spectroscopy (EDS) in Ref. [53], validating the present full multicomponent theory.

Competition between ferritic and austenitic growth from the melt was only reported at the boundaries of the melt pool, where the liquidus isotherm velocity is low and the temperature gradient is high. At the center of the melt pool, the microstructure suggests that only ferritic growth takes place, corresponding to increased velocity and decreased temperature gradient. However, the curves drawn in Figure 11a for $G = 10^7\ \mathrm{K}\cdot\mathrm{m}^{-1}$ suggest the selection of $\gamma-$austenite at high velocities, and thus do not explain the observations. Godfrey et al. addressed this by considering both the effect of the velocity and the temperature gradient on the dendrite tip kinetics. The additional effect of the temperature gradient on the dendrite tip temperature is shown in Figure 12. Table 7 reports the predicted velocity interval defined for non-plane-front growth, i.e., the lower limit of constitutional supercoolings, v_c, and the absolute stability limit, v_a, and the corresponding solidus temperature at various values of the temperature gradient. The absence of values in Table 7 means that no solution was found for non-plane-front growth from the melt. In other words, only planar-front solidification is possible at $G = 10^8\ \mathrm{K}\cdot\mathrm{m}^{-1}$ for $\gamma-$austenite and at $G = 10^9\ \mathrm{K}\cdot\mathrm{m}^{-1}$ for both $\delta-$ferrite and $\gamma-$austenite. In the latter case, because the solidus temperature for planar $\delta-$ferrite is always lower than for planar $\gamma-$austenite, only $\gamma-$austenite growth should be selected at $G = 10^9\ \mathrm{K}\cdot\mathrm{m}^{-1}$. This is due to the fact that the phase boundaries are independent of the temperature gradient: the computed non-equilibrium liquidus temperature and solidus temperature in Figure 11a are simply reproduced in Figure 12. Figure 12 also reproduces the effect of the temperature gradient known from classical theory, in which v_c is proportional to G and changes in G only affect this low-velocity regime of non-planar growth. Thus, as shown by Figure 12, the onset of non-plane-front solidification is always higher for $\gamma-$austenite compared to $\delta-$ferrite.

At the boundary of the melt pool, where the isotherm velocity and temperature gradient are typically $10^{-2}\ \mathrm{m}\cdot\mathrm{s}^{-1}$ and $10^8\ \mathrm{K}\cdot\mathrm{m}^{-1}$, respectively, $\gamma-$austenite is able to compete with $\delta-$ferrite. Indeed, Figure 12 shows that plane-front solidification is expected for the two microstructures, but note that the solidus temperature for $\gamma-$austenite is higher than that for $\delta-$ferrite. Thus, if $\gamma-$austenite was the initial solid-state microstructure, it could survive the competition against $\delta-$ferrite close to the vicinity of the melt pool boundaries. Hence, the role of the temperature gradient in the interpretations of the observed microstructure is a common feature with the work by Godfrey et al. [53]. However, we note the following differences from their analysis. First, their solidus temperature for $\delta-$ferrite is higher than for $\gamma-$austenite at all velocities, which contradicts the results using TCFE10 [51], even for the equilibrium behavior at low

Temperature gradient G [K · m^{-1}]		$\delta-$ferrite Velocity [m · s^{-1}]	$\delta-$ferrite Temperature T_S [K]		$\gamma-$austenite Velocity [m · s^{-1}]	$\gamma-$austenite Temperature T_S [K]
10^6	v_c	$1.25 \cdot 10^{-4}$	1690.14	v_c	$3.15 \cdot 10^{-4}$	1700.06
10^7		$1.32 \cdot 10^{-3}$	1690.14		$4.59 \cdot 10^{-3}$	1700.09
10^8		$2.18 \cdot 10^{-2}$	1690.42		–	–
10^9		–	–		–	–
	v_a	0.290	1693.52	v_a	0.128	1700.71

Table 7: Predicted velocity interval, $[v_c, v_a]$, for non plane-front growth in 316L stainless steel for the $\delta-$ferrite phase and the $\gamma-$austenite phase, together the corresponding interface temperature. Dashes indicate that a solution was not found for dendritic growth at the given thermal gradient.

velocities. It has been checked that addition of the minor elements Co, N, O, and P in the calculation of the equilibrium phase diagram boundaries does not change this result. Second, their model is calibrated to predict the FCC structure by increasing the diffusion coefficient in the liquid when computing the growth kinetics of $\delta-$ferrite by one order of magnitude from the value used for $\gamma-$austenite. This results in values of v_c that are consistently higher for $\delta-$ferrite than for $\gamma-$austenite, which is opposite to the behavior observed in Figure 12 and Table 7. As mentioned before, the temperature difference between the growth temperatures of the two phases from the melt is only a few Kelvin, which does not justify such a drastic adjustment of the diffusion coefficient.

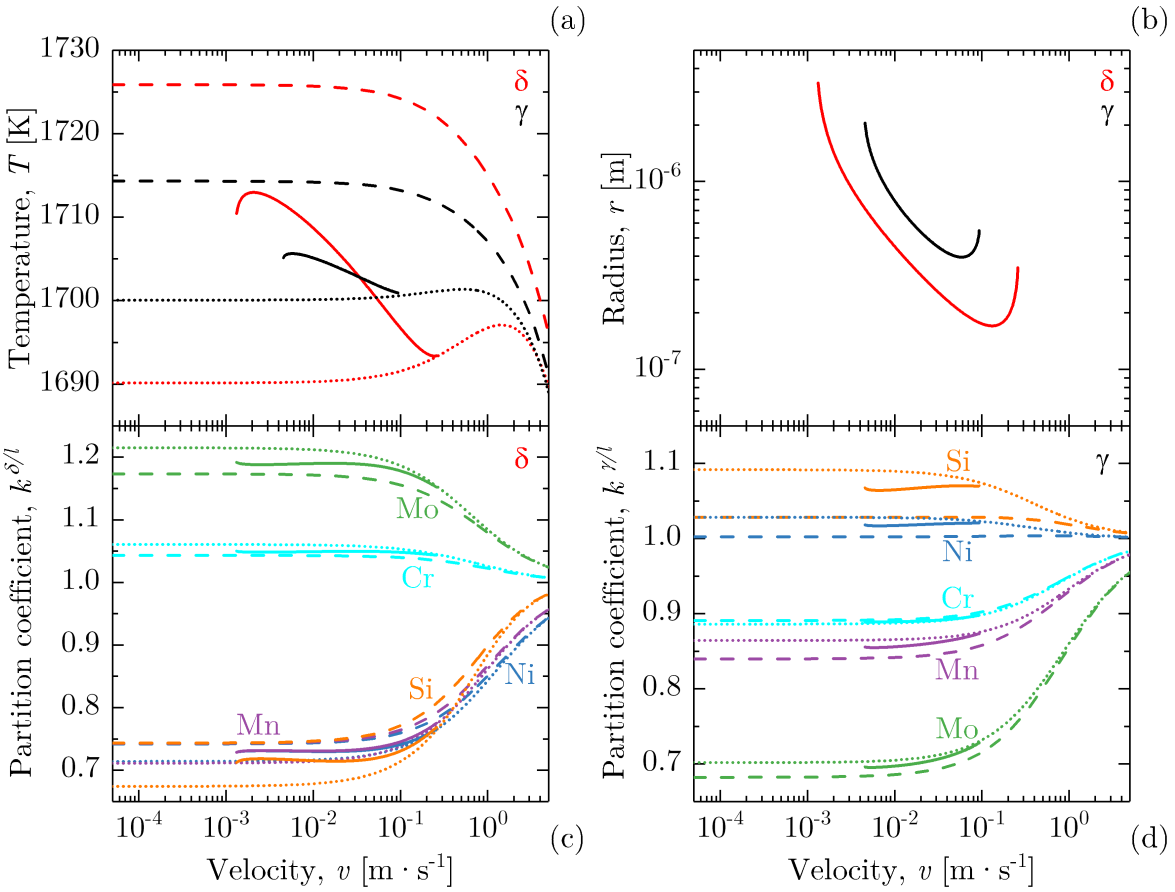

Figure 11: Dendrite tip kinetics for the $\delta-$ferrite phase and the $\gamma-$austenite phase of the 316L alloy of composition [wt%] Fe–16.81 Cr–11.92 Ni–2.43 Mo–0.99 Mn–0.36 Si [53] with the material parameters in Table 6 using PDM by Hareland *et al.* [23] and $G = 10^7$ K · m^{-1}: (a, solid) dendrite tip temperature, T_d, (b) tip radius, r, (c–d) partition coefficients for $\delta-$ferrite, $k^{\delta/l}$ [wt%·wt%$^{-1}$], and $\gamma-$austenite, $k^{\gamma/l}$ [wt%·wt%$^{-1}$], respectively, at (dashed) the liquidus temperature, (dotted) the solidus temperature and (solid) the dendrite tip temperature.

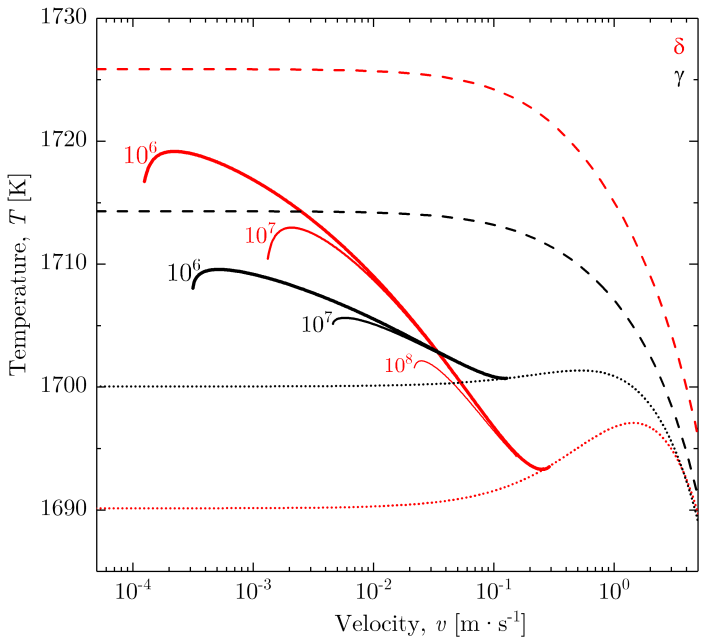

Figure 12: Dendrite tip temperature, T_d, for (red) the $\delta-$ferrite phase and (black) the $\gamma-$austenite phase of the 316L alloy of composition [wt%] Fe–16.81 Cr–11.92 Ni–2.43 Mo–0.99 Mn–0.36 Si [53] with the material parameters in Table 6 using PDM by Hareland *et al.* [23] and temperature gradient from (Thick) $G = 10^6\,\mathrm{K}\cdot\mathrm{m}^{-1}$ to (thin) $G = 10^8\,\mathrm{K}\cdot\mathrm{m}^{-1}$, with (dashed) liquidus temperature and (dotted) solidus temperature.

5. Conclusions

A model for multicomponent dendritic growth incorporating the effects of interfacial non-equilibrium and partial solute drag has been developed and coupled with CALPHAD methodology. The present Partial Drag Model (PDM) features a thermodynamically self-consistent treatment of partial solute drag, which leads to deviations from the classical Continuous-Growth Model (CGM) [2, 3, 4], especially for small values of the solute-drag parameter. In the present model for dendritic growth, increasing solute drag depresses the tip temperature from its equilibrium value and decreases the absolute stability limit.

Applications to industrial alloys are discussed: the model is used to calculate a velocity/undercooling relation for the non-equilibrium solidification of IN718, demonstrating the importance of considering the implementation of kinetics developed for concentrated multicomponent alloys versus applying those for a dilute-ideal solution. Phase selection in 316L stainless steel is also discussed. The model is used to understand previously reported microstructure selection during additive manufacturing using laser powder bed fusion [53]. Compared to previous interpretations, which also assume the phase formed from the liquid is that with the highest interfacial temperature, we do not require any adjustment of the phase diagram properties, the values of the diffusion coefficients of the chemical species, nor the Gibbs-Thomson coefficient (needed to account for the effect of curvature). Additionally, the present work computes the kinetic phase diagram directly and does not rely on the dilute-ideal approximations of the CGM. Therefore, the interpretations of the role of the solidification velocity and temperature gradient on the primary solidification microstructure are more consistent using the present model.

Experimental comparisons with multicomponent alloys are needed to ensure the accuracy of the model and the chosen kinetic parameters. This might require indirect comparisons with experimental data, such as the work started to couple the computation of solidification paths with the dendrite tip undercooling during rapid solidification in order to improve the descriptions of the fraction of interdendritic phases [64]. While this work is primarily motivated by the advent of additive manufacturing processes, it could also serve for analyses of levitated droplet experiments for which very high levels of undercooling can be reached prior to solidification. This will require the addition of the diffusion field for energy, as proposed by Lipton et al. [65], but will enable the comparison to the large amount of readily available experimental data. This would be beneficial, as most interpretations of undercooled melt solidification for multicomponent alloys still rely on multilinear phase diagram properties and ideal-dilute approximations for the non-equilibrium effects [7]. However, in this regime of ultra-rapid solidification, it is necessary to consider the effects of local non-equilibrium diffusion [66, 67]. A model combining the effects of partial solute drag and local non-equilibrium diffusion and coupled with CALPHAD methodology would thus be a powerful tool to characterize solidification at any interface velocity.

Appendix A: Interfacial response functions

- *Velocity Response Function (VRF)*

The velocity of the interface, v, is assumed proportional to the driving force for interface migration

through the interfacial mobility, $M^m = v_0/(RT)$, giving the VRF [23]:

$$v = \frac{v_0}{RT} \sum_{i=1}^{N} x_i^{eff} [\![\mu_i]\!] \tag{A.1}$$

• *Concentration Response Function (CRF)*

For an N-component alloy with solute elements $i \in \{1 : N-1\}$ and balance element $i = N$, the flux of component i due to trans-interface diffusion, J_i^t [$\mathrm{mol \cdot m^{-2} \cdot s^{-1}}$], is related to the driving force for trans-interface diffusion via [23]:

$$J_i^t = -\rho_0 \sum_{j=1}^{N} M_{ij}^t ([\![\mu_j]\!] - [\![\mu_N]\!]) \tag{A.2}$$

where the M_{ij}^t coefficients [$\mathrm{mol \cdot s \cdot m^{-1} \cdot kg^{-1}}$] represent the mobility of component i across the interface:

$$M_{ij}^t = x_i^{eff} \left(\delta_{ij} - x_j^{eff}\right) \frac{v_i^D}{RT} \tag{A.3}$$

Assuming a no-flux condition in the solid phase, the mass balance for component i at the solid/liquid interface gives [23]:

$$J_i^t = \rho_0 v \left(x_i^{eff} - x_i^{sl}\right) \tag{A.4}$$

Combining Eqs. (A.2)–(A.4), the CRF becomes:

$$v \left(x_i^{eff} - x_i^{sl}\right) = \frac{x_i^{eff} v_i^D}{RT} \sum_{j=1}^{N} (\delta_{ij} - x_j^{eff})([\![\mu_N]\!] - [\![\mu_j]\!]) \tag{A.5}$$

$$v \left(x_i^{eff} - x_i^{sl}\right) = \frac{x_i^{eff} v_i^D}{RT} \left([\![\mu_N]\!] - [\![\mu_i]\!] - \sum_{j=1}^{N} x_j^{eff} ([\![\mu_N]\!] - [\![\mu_j]\!])\right) \tag{A.6}$$

$$v \left(x_i^{eff} - x_i^{sl}\right) = \frac{x_i^{eff} v_i^D}{RT} \left([\![\mu_N]\!] - [\![\mu_i]\!] - \sum_{j=1}^{N} x_j^{eff} [\![\mu_N]\!] + \sum_{j=1}^{N} x_j^{eff} [\![\mu_j]\!]\right) \tag{A.7}$$

Using $\sum_{i=1}^{N} x_i^{eff} = 1$ reduces Eq. (A.7) to Eq. (6):

$$v \left(x_i^{eff} - x_i^{sl}\right) = \frac{x_i^{eff} v_i^D}{RT} \left(\sum_{j=1}^{N} x_j^{eff} [\![\mu_j]\!] - [\![\mu_i]\!]\right) \tag{6}$$

Finally, it is worth mentioning that substituting Eq. (A.1) in Eq. (6) leads to a combined form of the CRF:

$$v \left(x_i^{eff} - x_i^{sl}\right) = x_i^{eff} v_i^D \left(\frac{v}{v_0} - \frac{[\![\mu_i]\!]}{RT}\right) \tag{A.8}$$

Note, however, that Eq. (A.8) is still dependent on all $i \in \{1 : N-1\}$ independent components, as, in general, $\mu_i^\phi = \mu_i^\phi(T, \{x_i^\phi\})$ for phase ϕ. Comparison with the formulation of the IRFs by Aziz and Boettinger [4] for a binary alloy and by Du et al. [29] for a multicomponent alloy are provided in Table A.1.

		PDM	CGM
		Hareland *et al.* [23]	Aziz and Boettinger [4]
binary	VRF	$x_a^{eff}[\![\mu_a]\!] + x_b^{eff}[\![\mu_b]\!] = RT\dfrac{v}{v_0}$	$x_a^{eff}[\![\mu_a]\!] + x_b^{eff}[\![\mu_b]\!] = -RT\ln\left\{1-\dfrac{v}{v_0}\right\}$
	CRF	$v\left(x_b^{eff}-x_b^{sl}\right) = \dfrac{v^D x_b^{eff}}{RT}\left(1-x_b^{eff}\right)\left([\![\mu_a]\!]-[\![\mu_b]\!]\right)$	$v\left(x_b^{ls}-x_b^{sl}\right) = v^D(1-x_b^{ls})x_b^{sl}\left(1-\exp\left\{\dfrac{[\![\mu_b]\!]-[\![\mu_a]\!]}{RT}\right\}\right)$
		Hareland *et al.* [23]	Du *et al.* [29]
multi–component	VRF	$\displaystyle\sum_{i=1}^{N} x_i^{eff}[\![\mu_i]\!] = RT\dfrac{v}{v_0}$	$\displaystyle\sum_{i=1}^{N} x_i^{eff}[\![\mu_i]\!] = -RT\ln\left\{1-\dfrac{v}{v_0}\right\}$
	CRFs	$v\left(x_i^{eff}-x_i^{sl}\right) = \dfrac{v_i^D x_i^{eff}}{RT}\left(\displaystyle\sum_{j=1}^{N} x_j^{eff}[\![\mu_j]\!]-[\![\mu_i]\!]\right)$	$v\left(x_i^{ls}-x_i^{sl}\right) = v_i^D(1-x_i^{ls})x_i^{sl}\left(1-\exp\left\{\dfrac{[\![\mu_i]\!]-[\![\mu_N]\!]}{RT}\right\}\right)$

Table A.1: Summary of the Interfacial Response Functions (IRFs) — Velocity Response Function (VRF) and the Composition Response Functions (CRFs) — of the Partial-Drag Model (PDM) [23] incorporating partial solute drag and the Continuous-Growth Model (CGM) [4, 29]. In the IRFs corresponding to the binary alloy, the solvent is component a and the solute is component b. The solute-drag parameter λ is equivalent to the β parameter in the CGM models [4, 29].

Appendix B: molar flow versus mass flow

Guillemot et al. [24] presented a model for dendritic growth considering compositions in mass fraction, $(w_i)_{1\leq i\leq N-1}$ [(wt%)·(wt%)$^{-1}$]. Assuming a constant molar volume of the liquid, the solute fluxes, $\boldsymbol{\varphi}_{i,mass}$ [m·s^{-1}·(wt%)·(wt%)$^{-1}$], were expressed by:

$$\boldsymbol{\varphi}_{i,mass} = -\sum_{j=1}^{N-1} D_{ij}\boldsymbol{\nabla} w_j \tag{B.1}$$

However, the diffusion coefficients, $\mathbf{D} = (D_{ij})_{1\leq(i,j)\leq N-1}$ [m^2·s^{-1}], were defined for solute fluxes using compositions in mole fraction, $\boldsymbol{\varphi}_{i,mol}$ [m·s^{-1}·mol·(mol)$^{-1}$]:

$$\boldsymbol{\varphi}_{i,mol} = -\sum_{j=1}^{N-1} D_{ij}\boldsymbol{\nabla} x_j \tag{B.2}$$

where $(x_i)_{1\leq i\leq N-1}$ [mol $\cdot$ (mol)$^{-1}$]. Considering the following:

$$\boldsymbol{\varphi}_{i,mass} = \frac{M_i}{\{M\}}\boldsymbol{\varphi}_{i,mol} \tag{B.3a}$$

$$\boldsymbol{\varphi}_{i,mass} = -\frac{M_i}{\{M\}}\sum_{j=1}^{N-1} D_{ij}\boldsymbol{\nabla}x_j \tag{B.3b}$$

$$\boldsymbol{\varphi}_{i,mass} = -\frac{M_i}{\{M\}}\sum_{j=1}^{N-1} D_{ij}\frac{\{M\}}{M_j}\boldsymbol{\nabla}w_j \tag{B.3c}$$

$$\boldsymbol{\varphi}_{i,mass} = -\sum_{j=1}^{N-1} \underbrace{\frac{M_i}{M_j}D_{ij}}\boldsymbol{\nabla}w_j \tag{B.3d}$$

$$\boldsymbol{\varphi}_{i,mass} = -\sum_{j=1}^{N-1} D_{ij,mass}\boldsymbol{\nabla}w_j \tag{B.3e}$$

where $\{M\} = \sum_{i=1}^{N} x_i M_i$ is the average molar mass, it is apparent that Eq. (B.1) is only valid when the effects of cross-diffusion are neglected (i.e., when $D_{ij} = 0$ for $i \neq j$). Thus, the model computing the dendrite growth kinetics using mass fractions [24] was inaccurate, as all off-diagonal diffusion coefficients should have been corrected by the ratio M_i/M_j, as shown in equation (B.3d). The formulation used in this work corrects this issue and consistently uses mole fractions rather than mass fractions.

Data availability

All data included in this study are available upon reasonable request by contact with the corresponding author.

Declaration of competing interest

The authors declare that they have no known competing financial interests or personal relationships that could have appeared to influence the work reported in this paper.

Acknowledgements

PM acknowledges support from Safran Additive Manufacturing Campus (Mérignac, France). CAH acknowledges support from the National Science Foundation Graduate Research Fellowship (grant number DGE-1842165). CAH and PWV acknowledge the financial assistance award 70NANB14H012 from the U.S. Department of Commerce, National Institute of Standards and Technology as part of the Center for Hierarchical Materials Design (CHiMaD). PWV acknowledges support from the Fédération Doeblin for a visit at CEMEF, a research center of Mines Paris.

References

[1] W. Kurz, D. Fisher, R. Trivedi, Progress in modelling solidification microstructures in metals and alloys: dendrites and cells from 1700 to 2000, International Materials Reviews 64 (6) (2019) 311–354. doi:10.1080/09506608.2018.1537090.

[2] M. J. Aziz, Model for solute redistribution during rapid solidification, Journal of Applied Physics 53 (2) (1982) 1158–1168. doi:10.1063/1.329867.

[3] M. J. Aziz, T. Kaplan, Continuous growth model for interface motion during alloy solidification, Acta Metallurgica 36 (8) (1988) 2335–2347. doi:https://doi.org/10.1016/0001-6160(88)90333-1.

[4] M. Aziz, W. Boettinger, On the transition from short-range diffusion-limited to collision-limited growth in alloy solidification, Acta Metallurgica et Materialia 42 (2) (1994) 527–537. doi:10.1016/0956-7151(94)90507-X.

[5] W. Kurz, B. Giovanola, R. Trivedi, Theory of microstructural development during rapid solidification, Acta Metallurgica 34 (5) (1986) 823–830. doi:10.1016/0001-6160(86)90056-8.

[6] R. Trivedi, W. Kurz, Dendritic growth, Int. Mater. Rev. 39 (2) (1994) 49–74. doi:doi:10.1179/imr.1994.39.2.49.

[7] D. M. Herlach, Non-equilibrium solidification of undercooled metallic melts, Materials Science and Engineering R 12 (4-5) (1994) 177–272. doi:https://doi.org/10.1016/0927-796X(94)90011-6.

[8] A. Ludwig, The interface response-functions in multi-componental alloy solidification, Physica D: Nonlinear Phenomena 124 (1-3) (1998) 271–284. doi:10.1016/S0167-2789(98)00202-4.

[9] M. Bobadilla, J. Lacaze, L. G., Influence des conditions de solidification sur le déroulement de la solidification des aciers inoxydables austénitiques, Journal of Crystal Growth 89 (1988) 531—544. doi:https://doi.org/10.1016/0022-0248(88)90216-3.

[10] J. J. Hoyt, L. Wang, Layering misalignment and negative temperature dependence of interfacial free energy of b2-liquid interfaces in a glass forming system, Acta Materialia 219 (2011) 117259. doi:10.1016/j.actamat.2021.117259.

[11] K. Lücke, K. Detert, A quantitative theory of grain-boundary motion and recrystallization in metals in the presence of impurities, Acta Metallurgica 5 (11) (1957) 628–637. doi:10.1016/0001-6160(57)90109-8.

[12] M. Hillert, B. Sundman, A treatment of the solute drag on moving grain boundaries and phase interfaces in binary alloys, Acta Metallurgica 24 (8) (1976) 731–743. doi:10.1016/0001-6160(76)90108-5.

[13] M. Gurtin, P. Voorhees, The thermodynamics of evolving interfaces far from equilibrium, Acta Materialia 44 (1) (1996) 235–247. doi:10.1016/1359-6454(95)00139-X.

[14] Y. Yang, H. Humadi, D. Buta, B. B. Laird, D. Sun, J. J. Hoyt, M. Asta, Atomistic simulations of nonequilibrium crystal-growth kinetics from alloy melts, Physical Review Letters 107 (2) (2011) 025505. doi:10.1103/PhysRevLett.107.025505.

[15] S. Kavousi, B. R. Novak, J. Hoyt, D. Moldovan, Interface kinetics of rapid solidification of binary alloys by atomistic simulations: Application to Ti–Ni alloys, Computational Materials Science 184 (2020) 109854. doi:10.1016/j.commatsci.2020.109854.

[16] M. Haapalehto, T. Pinomaa, L. Wang, A. Laukkanen, An atomistic simulation study of rapid solidification kinetics and crystal defects in dilute Al–Cu alloys, Computational Materials Science 209 (2022) 111356. doi:10.1016/j.commatsci.2022.111356.

[17] E. Antillon, C. A. Hareland, P. W. Voorhees, Solute trapping and solute drag during non-equilibrium solidification of Fe–Cr alloys, Acta Materialia 248 (2023) 118769. doi:10.1016/j.actamat.2023.118769.

[18] A. Papapetrou, Untersuchungen über dendritisches Wachstum von Kristallen, Zeitschrift für Kristallographie - Crystalline Materials 92 (1-6) (1935) 89–130, publisher: De Gruyter (O). doi:10.1524/zkri.1935.92.1.89.

[19] G. P. Ivantsov, Temperature field around a spherical, cylindrical, and needle-shaped crystal, growing in a pre-cooled melt, Dokl. Akad. Nauk SSSR 58 (4) (1947) 567–569.

[20] W. W. Mullins, R. F. Sekerka, Stability of a planar interface during solidification of a dilute binary alloy, Journal of Applied Physics 35 (2) (1964) 444–451, publisher: American Institute of Physics. doi:10.1063/1.1713333.

[21] J. S. Langer, H. Müller-Krumbhaar, Stability effects in dendritic crystal growth, Journal of Crystal Growth 42 (1977) 11–14. doi:10.1016/0022-0248(77)90171-3.

[22] W. A. Tiller, K. A. Jackson, J. W. Rutter, B. Chalmers, The redistribution of solute atoms during the solidification of metals, Acta Metallurgica 1 (4) (1953) 428–437. doi:10.1016/0001-6160(53)90126-6.

[23] C. A. Hareland, G. Guillemot, C. A. Gandin, P. W. Voorhees, The thermodynamics of non-equilibrium interfaces during phase transformations in concentrated multicomponent alloys, Acta Materialia 241 (2022) 118407. doi:10.1016/j.actamat.2022.118407.

[24] G. Guillemot, O. Senninger, C. A. Hareland, P. W. Voorhees, C.-A. Gandin, Thermodynamic coupling in the computation of dendrite growth kinetics for multicomponent alloys, Calphad 77 (2022) 102429. doi:10.1016/j.calphad.2022.102429.

[25] Thermocalc database TCNI10 \Ni-Alloys v10.0, Thermo-Calc Software AB, Sweden (2020).
URL https://thermocalc.com

[26] Thermocalc database MOBNI5 \Ni-Alloys Mobility v5.1 , Thermo-Calc Software AB, Sweden (2019).
URL https://thermocalc.com

[27] O. Hunziker, Theory of plane front and dendritic growth in multicomponent alloys, Acta Materialia 49 (20) (2001) 4191–4203. doi:10.1016/S1359-6454(01)00313-5.

[28] V. S. Hariharan, B. S. Murty, G. Phanikumar, Interface response functions for multicomponent alloy solidification- An application to additive manufacturing (2023). doi:10.48550/arXiv.2303.07663.

[29] Q. Du, A. S. Azar, M. M'Hamdi, Kinetic interface condition phase diagram for the rapid solidification of multicomponent alloys with an application to additive manufacturing, Calphad 76 (2022) 102365. doi:10.1016/j.calphad.2021.102365.

[30] M. Hillert, Solute drag, solute trapping and diffusional dissipation of gibbs energy. this paper is based on the hume–rothery lecture presented at the 128th tms annual meeting, 1 march 1999, san diego, u.s.a., Acta Materialia 47 (18) (1999) 4481–4505. doi:https://doi.org/10.1016/S1359-6454(99)00336-5.

[31] J. C. Baker, J. W. Cahn, Thermodynamics of Solidification, American Society for Metals, Metals Park, Ohio, USA, 1971.

[32] R. W. Cahn, P. Haasen, Physical metallurgy, 4th Edition, North-Holland, Amsterdam, 1996, oCLC: 924676656.

[33] M. Ben Amar, E. Brener, Theory of pattern selection in three-dimensional nonaxisymmetric dendritic growth, Physical Review Letters 71 (1993) 589–592. doi:10.1103/PhysRevLett.71.589.

[34] E. Brener, Needle-crystal solution in three-dimensional dendritic growth, Physical Review Letters 71 (1993) 3653–3656. doi:10.1103/PhysRevLett.71.3653.

[35] J. S. Langer, Existence of needle crystals in local models of solidification, Physical Review A 33 (1) (1986) 435 – 441.

[36] D. A. Kessler, J. Koplik, H. Levine, Pattern selection in fingered growth phenomena, Advances in Physics 37 (3) (1988)

255–339. doi:10.1080/00018738800101379.

[37] P. Pelcé, Dynamics of Curved Fronts, 1st Edition, Academic Press, 1988.

[38] E. Brener, V. Mel'nikov, Pattern selection in two-dimensional dendritic growth, Advances in Physics 40 (1) (1991) 53–97. doi:10.1080/00018739100101472.

[39] J. Liu, J. Zou, M. Guo, N. Moelans, Phase-field simulation and analytical modelling of CaSiO3 growth in CaO-Al2O3-SiO2 melts, Computational Materials Science 144 (2018) 126–132. doi:https://doi.org/10.1016/j.commatsci.2017.12.018.

[40] A. Lahiri, A. Choudhury, Dendrite tip selection during isothermal free growth in multi-component alloys: Marginal stability theories and insights from phase-field simulations,, Computational Materials Science 158 (2019) 209–218. doi:https://doi.org/10.1016/j.commatsci.2018.11.028.

[41] J. S. Langer, H. Müller-Krumbhaar, Theory of dendritic growth—I. Elements of a stability analysis, Acta Metallurgica 26 (11) (1978) 1681–1687. doi:10.1016/0001-6160(78)90078-0.

[42] D. Coates, S. Subramanian, G. R. Purdy, Solid-liquid interface stability during solidification of dilute ternary alloys, Transactions of the Metallurgical Society of AIME 242 (1968) 800.

[43] S. Coriell, R. Sekerka, Oscillatory morphological instabilities due to non-equilibrium segregation, Journal of Crystal Growth 61 (3) (1983) 499–508. doi:10.1016/0022-0248(83)90179-3.

[44] S. Coriell, G. McFadden, Morphological Stability, in: Handbook of Crystal Growth, 1st Edition, Vol. 1b, Elsevier, 1993, pp. 785–858.

[45] R. Sekerka, S. Coriell, G. McFadden, Morphological Stability, in: Handbook of Crystal Growth, 2nd Edition, Vol. 1b, Elsevier, 2015, pp. 595–630. doi:10.1016/B978-0-444-56369-9.00014-9.

[46] A. Ludwig, B. Pustal, D. M. Herlach, General concept for a stability analysis of a planar interface under rapid solidification conditions in multi-component alloy systems, Materials Science and Engineering: A 304-306 (2001) 277–280. doi:10.1016/S0921-5093(00)01451-9.

[47] Thermocalc database TCAL4 \Al-Alloys version 4.0, Thermo-Calc Software AB, Sweden (2015).
URL https://thermocalc.com

[48] Thermocalc database MOBAL3 \Al-Alloys Mobility version 3.0, Thermo-Calc Software AB, Sweden (2013).
URL https://thermocalc.com

[49] Z. Jian, K. Kuribayashi, W. Jie, Solid-liquid interface energy of metals at melting point and undercooled state, Materials Transactions 43 (4) (2002) 721–726. doi:https://doi.org/10.2320/matertrans.43.721.

[50] D. Tourret, J. Klemm-Toole, A. E. Castellanos, B. Rodgers, G. Becker, A. Saville, B. Ellyson, C. Johnson, B. Milligan, J. Copley, R. Ochoa, A. Polonsky, K. Pusch, M. P. Haines, K. Fezzaa, T. Sun, K. Clarke, S. Babu, T. Pollock, A. Karma, A. Clarke, Morphological stability of solid-liquid interfaces under additive manufacturing conditions, Acta Materialia 250 (2023) 118858. doi:10.1016/j.actamat.2023.118858.

[51] Thermocalc database TCFE10 \Fe-Alloys, v10.1, Thermo-Calc Software AB, Sweden (2020).
URL https://thermocalc.com

[52] Thermocalc database MOBFE5 \Fe-Alloys Mobility, v5.0, Thermo-Calc Software AB, Sweden (2019).
URL https://thermocalc.com

[53] A. J. Godfrey, J. Simpson, D. Leonard, K. Sisco, R. R. Dehoff, S. S. Babu, Heterogeneity and solidification pathways in additively manufactured 316L stainless steels, Metallurgical and Materials Transactions A 53 (9) (2022) 3321–3340. doi:10.1007/s11661-022-06747-6.

[54] Z. Wang, K. Guan, M. Gao, X. Li, X. Chen, X. Zeng, The microstructure and mechanical properties of deposited-IN718 by selective laser melting, Journal of Alloys and Compounds 513 (2012) 518–523. doi:10.1016/j.jallcom.2011.10.107.

[55] M. Hillert, Phase Equilibria, Phase Diagrams and Phase Transformations: Their Thermodynamic Basis, Cambridge University Press, Cambridge, UK, 1998.

[56] J. W. Elmer, S. M. Allen, T. W. Eagar, Microstructural development during solidification of stainless steel alloys, Metallurgical Transactions A 20 (10) (1989) 2117–2131. doi:10.1007/BF02650298.

[57] J. A. Brooks, M. I. Baskes, F. A. Greulich, Solidification modeling and solid-state transformations in high-energy density stainless steel welds, Metallurgical Transactions A 22 (4) (1991) 915–926. doi:10.1007/BF02659001.

[58] S. Fukumoto, W. Kurz, The δ to γ transition in Fe-Cr-Ni alloys during laser treatment, ISIJ International 37 (7) (1997) 677–684. doi:10.2355/isijinternational.37.677.

[59] P. Bajaj, A. Hariharan, A. Kini, P. Kürnsteiner, D. Raabe, E. A. Jägle, Steels in additive manufacturing: A review of their microstructure and properties, Materials Science and Engineering: A 772 (2020) 138633. doi:10.1016/j.msea.2019.138633.

[60] H. Yasuda, K. Morishita, M. Yoshiya, T. Narumi, Transformation from ferrite to austenite during/after solidification in peritectic steel systems: An X-ray imaging study, ISIJ International 60 (12) (2020) 2755–2764. doi:10.2355/isijinternational.ISIJINT-2020-486.

[61] S. Astafurov, E. Astafurova, Phase composition of austenitic stainless steels in additive manufacturing: A review, Metals 11 (7) (2021) 1052. doi:10.3390/met11071052.

[62] H.-H. König, N. H. Pettersson, A. Durga, S. Van Petegem, D. Grolimund, A. C. Chuang, Q. Guo, L. Chen, C. Oikonomou, F. Zhang, G. Lindwall, Solidification modes during additive manufacturing of steel revealed by high-speed X-ray diffraction, Acta Materialia 246 (2023) 118713. doi:10.1016/j.actamat.2023.118713.

[63] Thermocalc software, Thermo-Calc Software AB, Sweden (2021).
URL https://thermocalc.com

[64] P. Martin, G. Guillemot, M. Bellet, F. Pichot, N. Leriche, Y. Mayi, C.-A. Gandin, Solidification path for rapid solidification – Application to multicomponent alloys for L-PBF, IOP Conference Series: Materials Science and Engineering 1281 (1) (2023) 012062, publisher: IOP Publishing. doi:10.1088/1757-899X/1281/1/012062.

[65] J. Lipton, W. Kurz, R. Trivedi, Rapid dendrite growth in undercooled alloys, Acta Metallurgica 35 (1987) 957–964. doi:10.1016/0001-6160(87)90174-X.

[66] P. Galenko, S. Sobolev, Local nonequilibrium effect on undercooling in rapid solidification of alloys, Physical Review E 55 (1) (1997) 343–352. doi:10.1103/PhysRevE.55.343.

[67] K. Wang, H. Wang, F. Liu, H. Zhai, Modeling dendrite growth in undercooled concentrated multi-component alloys, Acta Materialia 61 (11) (2013) 4254–4265. doi:10.1016/j.actamat.2013.03.051.